RSC Advances

PAPER

View Article Online
View Journal | View Issue

Cite this: *RSC Adv.*, 2026, **16**, 24719

Magnetically recoverable nano-adsorbents for dual removal of organic dyes and heavy metals from aqueous media

Olufemi Ogunjimi, John Verdaris, Fatema Tarannum, Kayla Foley and Keisha B. Walters *

Freshwater contamination by heavy metals and synthetic dyes poses serious environmental and health risks, driving the need for efficient, cost-effective, and recoverable remediation technologies. Magnetic nanoparticles (MNPs) have emerged as a promising platform due to their high surface area and easy magnetic recovery. However, tailoring their surface chemistry is essential to maximize pollutant uptake and reusability. In this work, functionalized Fe_3O_4 MNPs were developed *via* chemical co-precipitation followed by surface functionalization with 3-aminopropyl trimethoxysilane (APTES), glutaraldehyde (GA), and citric acid (CA), yielding MNP-APTES, MNP-APTES-GA, and MNP-CA, respectively, for the efficient removal of heavy metal ions and organic pollutants from aqueous solutions. Physicochemical characterization—including FTIR spectroscopy, dynamic light scattering and zeta potential, electron microscopy, and thermogravimetric analysis—confirmed successful surface modification without compromising magnetic properties of the Fe_3O_4 core. Adsorption performance was assessed for copper(II) ions (Cu^{2+}) in the presence of various competing heavy metal ions as well as for methyl orange (MO) dye. MNP-APTES-GA outperformed bare MNPs, MNP-CA, and MNP-APTES, achieving 69% Cu^{2+} removal at pH 6 and 83% MO decolorization at pH 3. Kinetic analysis demonstrated that Cu^{2+} uptake followed pseudo-first-order kinetics, whereas MO dye removal followed pseudo-second-order kinetics. The maximum Cu^{2+} adsorption capacity from the Langmuir model was 14.39 mg g^{-1}, and both Langmuir and Freundlich isotherms fit the experimental data well, suggesting heterogeneous, multilayer and competitive adsorption behavior. In multicomponent systems containing Co^{2+}, Ni^{2+}, Zn^{2+}, and Al^{3+}, Cu^{2+} removal remained 22–37%, confirming preferential Cu^{2+} uptake under competitive conditions. MNP regeneration experiments demonstrated robust reusability and good retention of adsorption capacity after five cycles using suitable eluents. Regeneration studies revealed strong reusability, with MO desorption remaining above 80% after five cycles, while Cu^{2+} desorption decreased from ~76% to ~30%. The enhanced dual-removal performance of MNP-APTES-GA is attributed to synergistic interactions from amine and aldehyde functionalities, enabling combined electrostatic attraction, coordination, and supramolecular interactions. These findings establish MNP-APTES-GA as a versatile, magnetically recoverable adsorbent with significant potential for scalable, multi-contaminant water remediation applications.

Received 3rd February 2026
Accepted 29th April 2026

DOI: 10.1039/d6ra00956e

rsc.li/rsc-advances

1. Introduction

Ensuring access to clean water is essential for human health and sustainable development. However, water pollution continues to rise due to rapid industrialization, population growth, and intensified domestic and agricultural activities, which when unabated contribute to the prevalence of life-threatening diseases.[1,2] Industrial effluents originating from textile,[3] chemical,[4] mining,[5] and metallurgical[6] sectors discharge large quantities of hazardous substances such as dyes, heavy metals, and other hazardous pollutants into aquatic systems. These toxic contaminants cause severe ecological damage and present carcinogenic and mutagenic risks to human populations.[7] Therefore, increasing attention has been directed toward the development of efficient and sustainable strategies for removing hazardous dyes and toxic heavy metals from wastewater discharged by manufacturing industries.[8,9]

Various conventional remediation methods such as chemical precipitation, ion exchange, membrane filtration, coagulation, and flocculation[3,10–12] have been utilized for the removal of heavy metal ions and synthetic dyes from contaminated water. Although effective under certain conditions, these methods are often constrained by drawbacks, including high operational

Ralph E. Martin Department of Chemical Engineering, University of Arkansas, Fayetteville, AR, 72701, USA. E-mail: keisha.walters@uark.edu

costs, secondary sludge production, membrane fouling, and limited efficiency at low pollutant concentrations.[6,13] In addition, dye removal presents further challenges due to the structural stability, high solubility, and resistance to biodegradation of many azo and aromatic compounds. By comparison, adsorption stands out as one of the most attractive alternatives due to its high removal efficiency, cost-effectiveness, ease of use, potential for reuse, and suitability for large-scale water purification.[10,13–15] Among various adsorbent materials, magnetic nanoparticles (MNPs)—particularly iron oxides—have gained significant attention owing to their high specific surface area, chemical tunability, environmental compatibility, and excellent magnetic responsiveness, which enable efficient adsorption and facile separation from aqueous systems without filtration or centrifugation.[16–19] Iron oxide based nano-adsorbents such as hematite (α-Fe_2O_3), maghemite (γ-Fe_2O_3), and magnetite (Fe_3O_4) have been widely explored for the remediation of toxic metal ions including arsenic (As^{3+}/As^{5+}),[20,21] chromium (Cr^{3+}/Cr^{4+}/Cr^{6+}),[22–24] manganese (Mn^{2+}),[25] copper (Cu^{2+}),[26] lead (Pb^{2+}),[27,28] and mercury (Hg^{2+})[29,30] from both environmental and industrial waste streams.[31–35] Magnetic recoverability of Fe_3O_4 makes it particularly attractive for sustainable wastewater treatment applications. In addition to metal ion removal, bare iron oxide nanoparticles have also demonstrated intrinsic adsorption capability toward various dye molecules such as methylene blue (MB),[36] methyl orange (MO),[37] Congo red (CR),[38] and rhodamine dyes.[39] However, unmodified Fe_3O_4 often suffer from aggregation due to magnetic dipole interactions and possess limited selectivity,[40] which reduces their adsorption efficiency in practical applications. To overcome these challenges, tailoring the surface chemistry of iron oxide-based MNPs has emerged as an effective strategy to improve their colloidal stability, target selectivity, and overall adsorption performance.[41,42]

Surface functionalization of iron oxide nanoparticles (IONPs) have been achieved using a variety of moieties such as silane coupling agents, organic vapor deposition, physiosorbed and chemisorbed polymers, and surfactants.[43,44] These modifications introduce functional groups capable of forming specific interactions with pollutant species while simultaneously preventing nanoparticle aggregation.[45] Among the different silane coupling agents, (3-aminopropyl)triethoxysilane (APTES) has been widely used due to its ability to form stable Fe–O–Si bonds with surface hydroxyl groups of Fe_3O_4 while exposing terminal amine ($-NH_2$) groups that serve as active sites for pollutant binding.[46] According to Campaña *et al.*, APTES-modified Fe_3O_4 NPs exhibited effective adsorption of Cd^{2+} ions from aqueous solution, achieving removal efficiencies up to 94% and a retention capacity of approximately 0.49 mg g^{-1}. Adsorption followed Langmuir/Freundlich isotherms and pseudo-first-order and pseudo-second-order kinetic models, which indicated APTES-modified Fe_3O_4 NPs as promising low-cost platforms for aqueous heavy metal remediation.[47] Besides silane-based functionalization, organic ligands such as citric acid (CA) have also been used to stabilize Fe_3O_4 nanoparticles through surface carboxylate groups.[48,49] CA-coated magnetite nanoparticles (Fe_3O_4-CA) were synthesized specifically as effective adsorbents for cadmium (Cd^{2+}) removal from aqueous solutions.[50] The adsorption performance of Cd^{2+} was systematically evaluated with different pH, temperature, and contact time. Equilibrium in Cd^{2+} adsorption onto Fe_3O_4-CA was achieved within 35 min at an optimized pH of 5, confirming the rapid adsorption kinetics. Similarly, Tziro and Baseri[51] investigated magnetite nano-adsorbents synthesized *via* chemical co-precipitation and subsequently coated with different organic and inorganic materials, including CA, for the adsorption of $Cu^{2+}$and Pb^{2+}. While bare Fe_3O_4 exhibited removal efficiencies of approximately 75% for Pb^{2+} and 78% for Cu^{2+}, CA-coated Fe_3O_4 NPs achieved removal efficiencies above 90%, confirming the pivotal role of surface charge and ligand coordination in metal binding.

Beyond heavy metals, functionalized iron-based nanomaterials have demonstrated high efficiency in dye removal and multifunctional applications. Yan and Wang synthesized amino-functionalized Fe_3O_4 nanoparticles *via* APTES modification and demonstrated effective adsorption of anionic dyes, achieving maximum capacities of 51.4 mg g^{-1} for Reactive Red 228 and 118.8 mg g^{-1} for CR.[52] Keshta and Gemeay[53] synthesized Fe_3O_4 nanoparticles using different methods (co-precipitation, hydrothermal, and sonochemical) and subsequently modified with APTES to introduce surface amine ($-NH_2$) groups, resulting in enhanced adsorption of the anionic dye Eosin-Y with a maximum adsorption capacity of 38.32 mg g^{-1}. In another study, amino-functionalized silica-coated Fe_3O_4 nanoparticles were synthesized and found effective for dye adsorption such as CR and MB, which indicated the versatility of amine-modified magnetic cores in treating different organic pollutants.[54] Alqadami *et al.* prepared trisodium-citrate-functionalized Fe_3O_4 (Fe_3O_4@TSC) which showed a maximum adsorption capacity of 435 mg g^{-1} for malachite green, demonstrating the strong adsorption capability imparted by citrate-derived surface carboxylate groups.[55] The same citrate-modified Fe_3O_4-TSC NPs also showed rapid and efficient adsorption of Cr^{3+} and Co^{2+}, with equilibrium adsorption capacities of 50 mg g^{-1} for Cr^{3+} and 47.4 mg g^{-1} for Co^{2+}.[56] The importance of carboxyl groups in adsorption processes is further illustrated by Qu *et al.*, who modified water hyacinth biomass with CA to introduce dense carboxyl functionalities. The systematic investigation of adsorption parameters (solution pH, contact time, initial adsorbate concentration, adsorbent dosage, and temperature) showed optimized conditions of pH 7.5 for Ni^{2+}, 6.0 for Cu^{2+}, and 5.0 for Cr^{2+}, with contact times of 300, 180, and 120 min, respectively.[57] These findings reinforce that carboxyl groups play a critical role in mediating selective ion binding, a principle directly translatable to iron oxide surfaces where carboxyl, amine, or hydroxyl groups can be tailored to maximize adsorption efficiency. Importantly, these parameter-specific optimizations provide a practical guideline for scaling up the adsorption process.[57] A comprehensive comparison of these studies, including adsorbent type, target pollutants, optimal pH conditions, adsorption capacities, and kinetic models, is summarized in Table 1, which provides a broader context for evaluating the performance of surface-functionalized Fe_3O_4-based adsorbents reported in the literature.

Table 1 Comparative adsorption performance of surface-functionalized Fe_3O_4 NPs for the removal of heavy metal ions and dye pollutants reported in the literature[a]

Adsorbent (with functional groups)	Pollutant	Optimal pH	Removal efficiency (%)	Adsorption capacity (mg g^{-1})	Kinetics/isotherm	Reference
Amine-functionalized Fe_3O_4	Cr^{4+} Ni^{2+}	3 6	95.25–97.94 96.42–98.56	232.51 222.12	Pseudo-second-order; Langmuir	Baghani *et al.*[58]
Carboxyl functionalized Fe_3O_4	Pb^{2+} Cd^{2+} Cu^{2+}	~5–5.5	—	74.63 45.66 44.84	Pseudo-second-order; Langmuir	Shi *et al.*[59]
EDTA-Fe_3O_4	Cu^{2+}	~5–6	~98.46 ± 0.08	~46.27	Pseudo-second-order; Langmuir	Liu *et al.*[60]
Fe_3O_4@SiO_2	Cd^{2+} Ni^{2+}	6	55 44	81.62 63.995	Langmuir and Freundlich	Ghafoor *et al.*[61]
APTES-GA-Fe_3O_4	Cu^{2+}	6	86	19.26	Pseudo-first-order; Langmuir isotherm	Özmen *et al.*[62]
Fe_3O_4-APTES	Cu^{2+}	4.0–5.3	78.2–79.6	61.07	Langmuir/Freundlich analyzed; fast equilibrium (~15 min)	Kothavale *et al.*[63]
Citric acid-coated Fe_3O_4	Crystal violet	~6–8	94.5%	~50–120	Pseudo-second-order; Langmuir	Jangra *et al.*[64]
Fe_3O_4–NH_2–COOH	Pb^{2+} Cd^{2+}	~5–6	96.8% 89.4%	125.3 98.7	Synergistic binding (dual sites)	Yang *et al.*[65]
Fe_3O_4-SDS	Tolonium chloride	6	98	111.11	Pseudo-second-order, Langmuir	Abedi *et al.*[66]
Fe_3O_4-APTES (amine-functionalized)	Reactive red 228 Congo red	~3–5 4–10	95.26 94.2	51.4 118.8	Pseudo-second-order Langmuir, Freundlich	Yan and Wang[52]
Fe_3O_4-APTES (amine-functionalized)	Eosin Y (EY)	~4–6 (best acidic)	~94–100	38.32	Pseudo-second-order Langmuir	Keshta & Gemeay[53]
Fe_3O_4-APTES-GA	Cu^{2+}	3	69%	21.39	Pseudo-first-order; Langmuir and Freundlich	This work
	Methyl orange	6	83%	17.95	Pseudo-second-order	

[a] SDS: sodium dodecyl sulfate; EDTA: ethylenediaminetetraacetic acid; GA: glutaraldehyde.

To further improve adsorption efficiency, dual-functional surface modification strategies combining different functional groups have also been explored. In many cases, APTES is used as an intermediate functionalization layer that introduces reactive amine groups and subsequently can react with aldehydes, carboxylic acids, or other functional molecules.[67] Karimi *et al.* synthesized Fe_3O_4 NPs sequentially modified with APTES and glutaraldehyde (GA), which introduced surface amine and aldehyde functional groups to provide abundant coordination sites for metal binding. The resulting Fe_3O_4/APTES/GA NPs exhibited superior adsorption of thorium ions (Th^{4+}) under optimized conditions of pH 4.5, 250 mg L^{-1} initial thorium concentration, 1 g L^{-1} adsorbent dosage, and 90 min contact time. The enhanced performance was attributed to the synergistic coordination of amine and aldehyde functionalities on the particle surface.[68] Similarly, Yang *et al.*[65] synthesized dual-functional amino–carboxyl co-modified Fe_3O_4 nanoparticles using APTES followed by succinic anhydride, which exhibited maximum adsorption capacities of 125.3 mg g^{-1} for Pb^{2+} and 98.7 mg g^{-1} for Cd^{2+}. It was attributed to the combined presence of amine and carboxyl functional groups that significantly enhances metal ion binding through cooperative coordination and electrostatic interactions. Özmen *et al.*[62] and Kothavale *et al.*[63] both developed APTES-glutaraldehyde (GA) functionalized Fe_3O_4 NPs for Cu^{2+} removal from aqueous solutions, where surface amine and imine groups introduced by APTES and GA provided active coordination sites. Özmen *et al.*[69] reported rapid adsorption kinetics with equilibrium reached within ~15 min and a high Langmuir adsorption capacity of 0.961 mmol g^{-1} (≈61.07 mg g^{-1}), whereas Kothavale *et al.*[63] observed ~86% Cu^{2+} removal at pH 6 with an

adsorption capacity of 19.26 mg g^{-1} and equilibrium reached within ~120 min, with the adsorption behavior fitting the Langmuir isotherm and pseudo-first-order kinetics. Despite these promising results, both studies are primarily limited to a single-component removal system, and their adsorption performance is strongly influenced by solution pH and competing ions, resulting in reduced efficiency under more complex conditions. In contrast, the present work extends beyond these limitations by demonstrating the simultaneous removal of Cu^{2+} ions and MO dye, thereby establishing a multifunctional adsorption platform. Furthermore, the inclusion of competitive multi-ion systems provides a more realistic evaluation of adsorbent performance, while the comparative analysis of different surface functionalization strategies offers deeper insight into the relationship between surface chemistry and adsorption behavior. These features highlight the enhanced versatility and practical applicability of the present system for wastewater treatment involving mixed contaminants.

In this study, Fe_3O_4 MNPs were synthesized *via* a one-pot co-precipitation and crosslinking strategy using 3-aminopropyl triethoxysilane (APTES), glutaraldehyde (GA), and citric acid (CA) to produce three functionalized materials-MNP-APTES, MNP-APTES-GA, and MNP-CA, respectively. The main objective of this work is to comparatively evaluate amine-, aldehyde/imine-, and carboxyl-functionalized IONPs to understand how different surface functionalization influence its adsorption behavior. The combination of surface functionalities is designed to synergistically enhance adsorption affinity, accelerate binding kinetics, and improve recyclability, thereby overcoming limitations of conventional single-ligand systems. The novelty of this work lies in the integration of multiple functional groups onto Fe_3O_4 MNPs to prepare MNP-APTES-GA and achieve remediation of both heavy metal (Cu^{2+}) and dye (MO) within a single platform—an advancement rarely reported in the literature.[63,69] In this study, Cu^{2+} was selected as a representative heavy metal due to its ubiquity in industrial effluents and high toxicity even at trace levels, while MO, a persistent azo dye, was chosen as a model organic contaminant owing to its persistence and resistance to biodegradation. Together, these pollutants reflect the realistic complexity of wastewater, where metals and dyes often coexist and require concurrent removal. Comprehensive characterization by Fourier transform infrared (FTIR) spectroscopy, zeta potential, thermogravimetric analysis (TGA), scanning electron microscopy (SEM), transmission electron microscopy (TEM), dynamic light scattering (DLS), X-ray diffraction (XRD), and ultraviolet-visible spectroscopy (UV-vis) confirms robust surface grafting without compromising magnetic responsiveness. These analyses provide structural, morphological, and functional verification of successful ligand immobilization. Furthermore, systematic evaluation of adsorption parameters, including contact time, pH, adsorbent dose, initial concentration, and coexisting ions, elucidated the adsorption pathways and maximized removal efficiencies. To elucidate the adsorption mechanisms, pseudo-first-order and pseudo-second-order kinetic models were applied to evaluate adsorption rates, while Langmuir and Freundlich isotherm models were used to analyze equilibrium adsorption behavior and surface interactions. To understand the adsorption mechanisms, pseudo-first-order and pseudo-second-order kinetic models were applied to evaluate the adsorption rates of Cu^{2+} and MO removal, while Langmuir and Freundlich isotherm models were used to analyze equilibrium adsorption behavior and surface interactions. Overall, by comparing APTES, APTES-GA, and CA functionalized Fe_3O_4 nanoparticles, this study provides a systematic understanding of how surface functionalization influences adsorption performance and recyclability in magnetic nanoadsorbents. Such scalable and reusable magnetic nanoparticles offer a promising and sustainable approach for the simultaneous removal of heavy metals and dyes from complex wastewater streams.

2 Materials and methods

2.1 Materials

Iron(III) chloride hexahydrate ($FeCl_3 \cdot 6H_2O$, CAS 7789-21-1, ≥99% ACS) and iron(II) chloride tetrahydrate ($FeCl_2 \cdot 4H_2O$, CAS 13478-10-9, ≥98%) were procured from Beantown Chemicals. Glutaraldehyde (GA, CAS 111-30-8, 25 wt% aqueous solution) and ethanol (anhydrous, CAS 64-17-5, ≥99.5%) were obtained from VWR Chemicals. 3-Aminopropyl triethoxysilane (APTES, CAS 919-30-2, ≥98%), ammonium hydroxide (NH_4OH, CAS 1336-21-6, 28–30 wt% NH_3 in H_2O), ethylenediaminetetraacetic acid (EDTA, CAS 6381-92-6, ≥99.5%, disodium salt), and citric acid monohydrate (CA, CAS 77-92-9, ≥99.5%) were purchased from Thermo Fisher Scientific. Copper(II) sulfate pentahydrate ($CuSO_4 \cdot 5H_2O$, CAS 7758-98-7, ≥99%), aluminum sulfate ($Al_2(SO_4)_3$, CAS 10043-01-3, ≥97%), nickel(II) sulfate hexahydrate ($NiSO_4 \cdot 6H_2O$, CAS 10101-97-0, ≥98%), cobalt(II) sulfate heptahydrate ($CoSO_4 \cdot 7H_2O$, CAS 10026-24-1, ≥98%), and zinc sulfate heptahydrate ($ZnSO_4 \cdot 7H_2O$, CAS 7446-20-0, ≥98%) were obtained from Sigma-Aldrich, and methyl orange dye (MO, CAS 547-58-0, ≥85% dye content) was purchased from LabChem, Inc. Deionized (DI) water was obtained from a MilliporeSigma water system. Branson SFX 150 ultrasonifier from Marshall Scientific was used to prevent aggregation during nanoparticle synthesis. All materials were used as received unless otherwise specified.

2.2 Synthesis of magnetic nanoparticles (MNP)

The reaction mechanism for the synthesis and surface functionalization of Fe_3O_4 magnetic nanoparticles is shown in Fig. 1. MNPs were prepared using an improved co-precipitation method with iron(III) chloride hexahydrate (6.5 g) and iron(II) chloride tetrahydrate (3.5 g) mixed in 100 mL of distilled water at 80 °C. NH_4OH (40 mL) was added dropwise and vigorously stirred into the solution under an inert atmosphere, with a rapid change in the solution colour from orange to black observed, indicating the formation of MNPs. The solution mixture was continuously stirred for an additional 30 min before proceeding to the washing step. The resulting black MNP particles were separated from the solution with a magnet and washed several times with deionized water and ethanol. Finally, a portion of the MNPs was redispersed into water while another portion was dispersed into ethanol for further characterization. The remainder was dried in an oven overnight at 40 °C[70] to produce Fe_3O_4 MNPs.

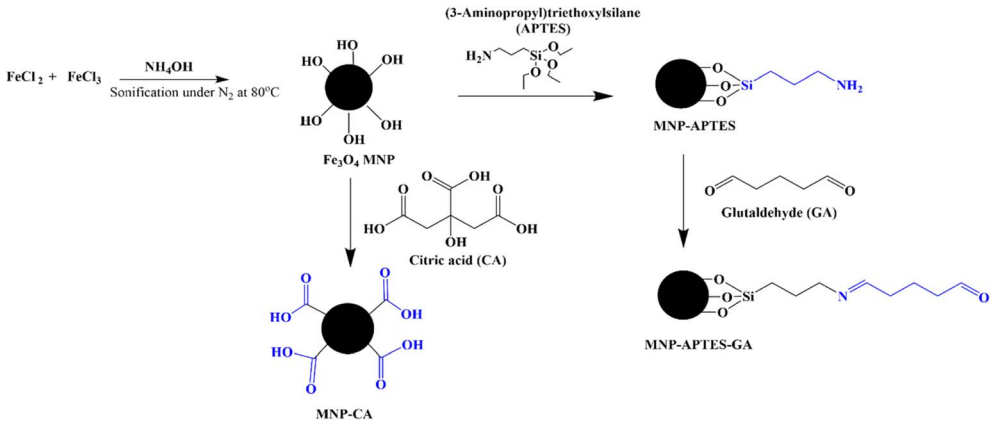

Fig. 1 Schematic illustration of the synthesis and surface functionalization of MNPs by 3-aminopropyl triethoxysilane (APTES), glutaraldehyde (GA), and citric acid (CA).

2.3 Surface modification of MNPs with 3-aminopropyl triethoxysilane (MNP-APTES)

Amino-functionalized MNPs were produced according to Ozmen *et al.*[69] Fe_3O_4 NPs (2 g) were dispersed in 100 mL of an ethanol/water solution (1 : 1 v/v ratio); afterward, 7.65 g of 3-aminopropyl triethoxysilane (APTES) was added to the solution with sonication under a nitrogen atmosphere at 40 °C for 2 h. The solution was then allowed to cool to room temperature, and the resulting MNP-APTES particles were separated from the solution using a permanent neodymium magnet. Aliquots of the particles were dispersed in ethanol for further characterization, while the remainder was dried in a vacuum oven overnight at 40 °C.

2.4 Surface modification of MNP-APTES with glutaraldehyde (MNP-APTES-GA)

MNP-APTES particles were further functionalized with glutaraldehyde (GA) based on the method described,[30,69] where APTES modified MNPs (2 g) were dispersed in a 75 mL solution containing 12.5 wt% GA and stirred for 12 h at room temperature. Subsequently, the resulting suspension was washed three times with ethanol, then the particles were separated and washed 3× with DI water and finally dried in a vacuum oven at 40 °C overnight to yield MNP-APTES-GA.

2.5 Surface modification of MNPs with citric acid (MNP-CA)

Fe_3O_4 MNPs were separately also surface modified with citric acid (CA) following a method by Dheyab *et al.*,[71] where 100 mL of CA was added to a mixture of 2 g of bare MNP in 25 mL of ethanol. This solution was stirred for 30 min at 65 °C. The resulting MNP-CA particles were then collected through a permanent magnet and thoroughly rinsed four times with DI water to remove unreactive or inert impurities. Finally, the MNP-CA was redispersed in the DI water for 10 min and magnetically decanted after sonication. The resultant particles were dried in the oven overnight at 40 °C.

2.6 Adsorption and desorption experiment

Adsorption studies were conducted to evaluate the removal of copper(II) sulfate pentahydrate and methyl orange (MO) using surface functionalized magnetic nanoparticles as adsorbents.

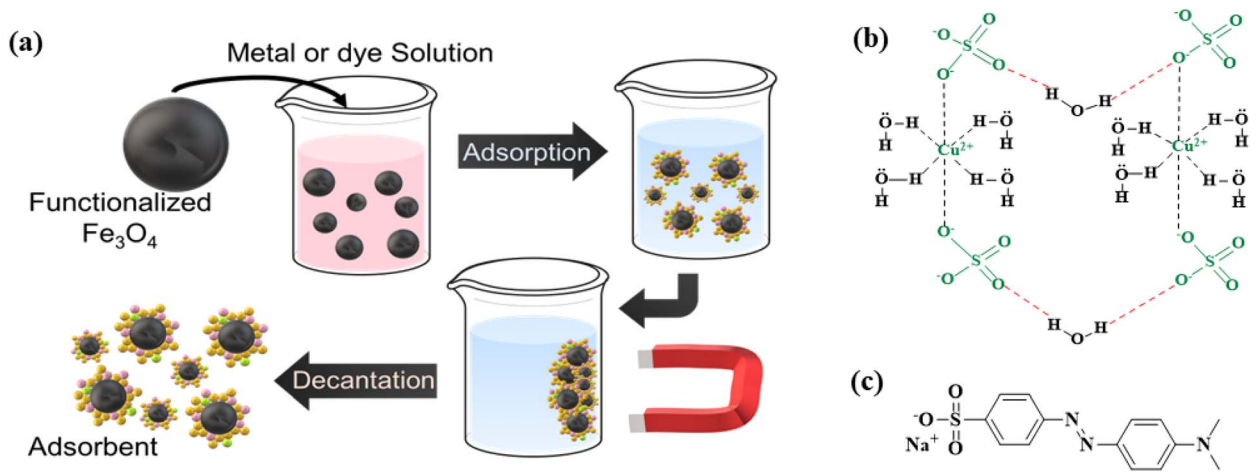

Fig. 2 (a) Schematic illustration of the adsorption and decantation process (adapted from Panda *et al.*[72]). Chemical structures of (b) copper(II) sulfate pentahydrate and (c) MO dye.

The residual concentration of Cu^{2+} ions was determined spectrophotometrically at 744 nm using ethylenediaminetetraacetic acid (EDTA) as a complexing agent, and the corresponding removal efficiency was calculated. For copper adsorption experiments, MNPs at a dosage of 5 g L^{-1} were placed in 500 mg L^{-1} (2 mM) Cu^{2+} ion solution and agitated in a shaker at 250 rpm and 25 °C for a specified time to attain adsorption equilibrium. For MO adsorption, an initial dye concentration of 45.8 mg L^{-1} (0.14 mM) was used.

To investigate the effect of key experimental factors, the rate of adsorption for the Cu^{2+} ions using MNPs was determined by varying contact time (30–210 min), adsorbent dose (2.5–15 g L^{-1} of MNPs), initial concentration (100–500 mg L^{-1}), and pH (3–7). For MO adsorption, the parameters of contact time (15–120 min), 2 g L^{-1} adsorbent dose, and pH (3, 5, 10) were studied. At the end of each batch experiment, MNPs were decanted using a permanent magnet. The adsorption experiments were repeated three times, and the average values were reported. Fig. 2 depicts the adsorption and desorption process using MNPs as the adsorbent along with the chemical structures of adsorbates.

The percentage adsorption conducted for Cu^{2+} and MO was deduced based on the following equations:

$$\%\ \text{Removal} = \frac{C_o - C_e}{C_o} \times 100 \quad (1)$$

where C_o (mg L^{-1}) is the initial adsorbate concentration, and C_e (mg L^{-1}) is the equilibrium adsorbate concentration. The adsorption capacity of the functionalized MNPs is expressed as follows:

$$\text{At equilibrium condition, } q_e = \frac{C_o - C_e}{m} \times V \quad (2)$$

$$\text{At any time}(t), \ q_t = \frac{C_o - C_t}{m} \times V \quad (3)$$

where q_e (mg g^{-1}) is the adsorption capacity at equilibrium, q_t (mg g^{-1}) is the adsorption capacity at time t (min), C_o (mg g^{-1}) is the initial concentration of the adsorbates, C_e (mg g^{-1}) is the adsorbate equilibrium concentration, C_t (mg L^{-1}) is the adsorbate concentration at time t (min), V (L) is the adsorbate volume, and m (g) is the weight of the adsorbents. The amount of Cu^{2+} adsorbed at time t was determined from the difference between the initial Cu^{2+} concentration and the concentration remaining in solution after adsorption.

Desorption and reusability studies were carried out after Cu^{2+} and MO adsorption using MNP-APTES-GA nanoparticles. For MO desorption, 2.5 g L^{-1} of MNP-APTES-GA was treated at pH 3, with a contact time of 60 min and an initial MO concentration of 45.8 mg L^{-1}. In accordance with Shariati-Rad *et al.*,[73] and Afkhami *et al.*,[74] 10 mL of 0.1 M NaOH was used as the eluent, followed by washing with distilled water before reuse. For Cu^{2+} desorption, MNP-APTES-GA (15 g L^{-1}) was applied at pH 6 with a contact time of 90 min and an initial Cu^{2+} concentration of 100 mg L^{-1}. Following literature reports,[75–77] 10 mL of 0.1 M HCl was used as the eluent, and the adsorbent was washed with distilled water before subsequent use. Dye concentration in the desorbed solution was measured spectrophotometrically.

The expression utilized for the desorption percentage was deduced from Zhai *et al.*[78] as follows,

$$\%\ \text{Desorption} = \frac{C_d}{C_a} \times 100\% \quad (4)$$

where C_d is the concentration of MO desorbed (mg L^{-1}), and C_a is the concentration of MO adsorbed (mg L^{-1}). The adsorption kinetics of Cu^{2+} and MO on MNP-APTES-GA were studied using pseudo-first-order and pseudo-second-order models to evaluate the adsorption rate and mechanism. Batch experiments were conducted by mixing a fixed mass of adsorbent in solution under optimized conditions, and residual solution concentrations were measured at discrete time intervals to calculate adsorption capacity (q_t). The pseudo-first-order kinetic model[79] is expressed as

$$\frac{dq}{dt} = k_1(q_e - q_t) \quad \text{(differential expression)} \quad (5)$$

$$\text{In}(q_e - q_t) = \text{In}\, q_e - k_1 t \ \text{(integral expression)} \quad (6)$$

where q_e (mg g^{-1}) is the equilibrium adsorption capacity, q_t (mg g^{-1}) is the adsorption capacity at t time, t is the adsorption time, and k_1 (min^{-1}) is the pseudo-first order kinetic adsorption rate constant. The pseudo-second-order model assumes that adsorption involves surface diffusion, surface adsorption, and particle diffusion, providing a more realistic description of the mechanism. The second-order equations are as follows:

$$\frac{dq}{dt} = k_2(q_e - q_t)^2 \quad \text{(differential equation)} \quad (7)$$

$$\frac{t}{q_t} = \frac{1}{k_2 q_e{}^2} + \frac{t}{q_e} \quad \text{(integral expression)} \quad (8)$$

where k_2 is the pseudo-second-order kinetic adsorption rate constant.

2.7 Adsorption isotherms

Adsorption isotherms are essential for evaluating the adsorption capacity of materials and understanding adsorbate–adsorbent interactions at equilibrium.[80–82] Among the most widely used models are the Langmuir, Freundlich, Temkin, and Dubinin–Radushkevich isotherms.[79] The Langmuir model assumes that adsorption occurs as a monolayer on a homogeneous surface with a finite number of identical binding sites,[83] and its linear form[79] is expressed as

$$\frac{C_e}{q_e} = \frac{C_e}{q_{m\,L}} + \frac{1}{K_L q_{m\,L}} \quad (9)$$

where C_e (mg L^{-1}) is the equilibrium concentration, q_e (mg g^{-1}) is the equilibrium adsorption capacity, $q_{m\ L}$ (mg g^{-1}) is the maximum saturated adsorption capacity, and K_L (L mg^{-1}) is the Langmuir adsorption constant related to the adsorption energy.

The Freundlich isotherm, in contrast, is an empirical model that assumes a heterogeneous surface with multilayer adsorption,[79] where adsorbate interactions occur and adsorption capacity increases with concentration; its linear form is given as

$$\ln q_e = \ln K_F + \frac{1}{n} \ln C_e \quad (10)$$

where K_F (L g^{-1}) is the Freundlich adsorption constant related to adsorption capacity and n is the Freundlich constant related to the degree of surface inhomogeneity.

2.8 Characterization methods

Fourier transform infrared spectroscopy (FTIR) was performed to characterize the surface functional groups of the MNPs using a ThermoFisher Scientific Nicolet iS50R FTIR spectrometer. To reduce water peak interference in the spectra, each sample was dried in a vacuum oven at 50 °C for 24 h before conducting the FTIR scans. FTIR spectra were collected over the 4000–400 cm^{-1} wavenumber range with an average of 64 scans at 4 cm^{-1} resolution and processed using OMNIC (Thermo Scientific™) software. The net surface charge of the nanoparticles was measured using an Anton Paar Litesizer 500 at room temperature, with each sample dispersed in an aqueous solution at 1 mg mL^{-1} concentrations.

Thermogravimetric analysis (TGA) of the MNPs was conducted with a Discovery TGA 5500 instrument (TA Instruments). Approximately 15 mg of each sample was heated from 25 to 800 °C at a rate of 10 °C min^{-1} under a nitrogen flow rate of 20 mL min^{-1}. The surface morphology of the samples was examined using scanning electron microscopy (SEM) on a Zeiss NEON high vacuum field-emission operated at an accelerating voltage of 15.00 kV.

Transmission electron microscopy (TEM) analysis was performed with a FEI Titan transmission electron microscope equipped with a field emission gun operating at 80 to 300 kV and an energy dispersive X-ray detector for elemental analysis. About 5 mg of each sample was ultrasonically dispersed in ethanol, and a drop of the suspension was deposited onto a carbon-coated copper grid and dried prior to imaging. A Shimadzu 1601 UV-Vis spectrophotometer was used to determine the concentration of anionic dye and Cu^{2+} in aqueous solution before, during, and after the adsorption process. Spectra were collected over the 1100–200 nm wavelength range at a spectral resolution of 1 nm. Calibration curves were produced by measuring the absorbance of a series of standard solutions with known concentrations of dye and Cu^{2+}. The equipment was baseline corrected with DI water at the respective corresponding analytical wavelengths to ensure accuracy before analyzing the adsorbate solutions.

X-ray diffraction (XRD) patterns were recorded using a Philips X'Pert MPD diffractometer equipped with a 1.8 kW Cu Kα X-ray tube (λ = 0.15406 nm), a 1/2° divergence slit, a 0.2 mm receiving slit, and a flat monochromator positioned in front of the standard proportional detector. The average crystallite size (D) of the nanoparticles was estimated using the Debye–Scherrer equation.[84]

$$D = \frac{k\lambda}{\beta \cos \theta} \quad (11)$$

where k is a shape factor (0.9), λ is the Cu Kα radiation wavelength (1.54060 Å), β is the peak width at half maximum (in radians), and θ is the Bragg diffraction angle.

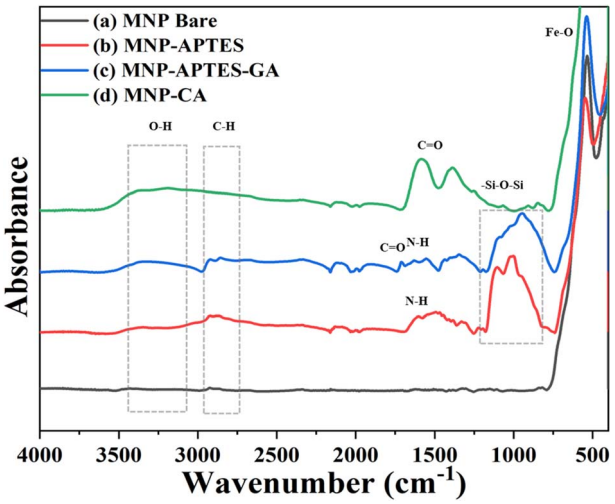

Fig. 3 FTIR spectra of magnetic nanoparticle samples: (a) bare MNP; (b) MNP-APTES; (c) MNP-APTES-GA; and (d) MNP-CA.

3 Results and discussion

3.1 Characterization of MNPs

To evaluate the chemical composition of the as-synthesized (bare) MNPs and examine the success of the surface functionalization using APTES, GA, and CA, FTIR spectroscopy was used to identify the characteristic vibrational bands for the functional groups present in each sample. Fig. 3a–d displays the FTIR spectra of bare and functionalized Fe_3O_4 nanoparticles. The FTIR spectra for bare MNPs do not show the presence of any functional groups at absorbances above 800 cm^{-1}, while an intense peak was observed at 537 cm^{-1} with this feature attributed to the Fe–O bond of bulk magnetite, as reported.[30] The lack of other functional groups and the strong Fe–O band indicated the successful formation of bare magnetite nanoparticles.

The surface modification of the MNPs with APTES was confirmed by the presence of the peaks at 1093 and 1031 cm^{-1} associated with Si–O groups, as well as two broad peaks at 1625 and 2927 cm^{-1}, which were assigned to N–H stretching and the C–H stretch of the anchored propyl group, respectively. Similar peaks have been previously reported for APTES coatings by Ozmen *et al.*[62] After the reaction of MNP-APTES with GA to obtain MNP-APTES-GA, a peak at 1709 cm^{-1} emerged, indicating the presence of the carbonyl group. Strong absorption bands at 937 and 1093 cm^{-1} were attributed to Si–O–Si groups, while peaks at 1625 and 1709 cm^{-1} were assigned to N–H stretching and C=O carbonyl vibrations, respectively. Additional bands at 2927 and 2848 cm^{-1} indicated the presence of the propyl group[63] for the MNP-APTES-GA, confirming that the APTES shell remained intact after the reaction with GA. In the FTIR spectra for MNP-CA, as shown in Fig. 3d, two strong bands at 1584 and 1387 cm^{-1} arise from vibrations of the citric-acid-derived carboxylate groups on the nanoparticle surface. Specifically, the 1584 cm^{-1} band corresponds to the asymmetric stretch of the $-COO^-$ moiety, while the 1387 cm^{-1} band is due to its symmetric stretch. All

MNP samples exhibited a broad absorption band between 3200 and 3400 cm^{-1}, characteristic of O–H stretching vibrations from surface hydroxyl groups.[85] These hydroxyls are attributed to hydrogen bonding between oxygen atoms on the Fe_3O_4 nanoparticles and adsorbed water molecules or hydrogen species. Additionally, the intense absorption at ~537 cm^{-1} is assignable to the Fe–O stretching vibration of the magnetite core. These spectral features confirm that citric acid was successfully grafted onto the MNP surface *via* its carboxylate functionalities, consistent with our group's previous observations and consistent with the work of Dheyab *et al.*[71]

In general, colloidal solutions with $|\zeta|$ > 30 mV are considered stable, while those with $|\zeta|$ > 60 mV demonstrate exceptional stability.[86] A high absolute zeta potential indicates that particles have a high net surface charge, which prevents particle aggregation due to charge repulsion. Conversely, colloidal solutions with $|\zeta|$ < 20 mV indicate poor stability, and those with a zeta potential between zero and ±5 mV tend to experience significant aggregation. Thus, the functionalized MNPs in this study exhibit superior suspension stability[69] compared to bare MNPs. At near-neutral zeta potential, attraction forces overcome repulsion, leading to agglomeration; however, when two adjacent particles have sufficiently high zeta potential of the same sign, they do not agglomerate due to electrostatic repulsions. The results of this study clearly indicate that surface modification and functionalization significantly increase zeta potential, thereby enhancing colloidal stability, with the notable exception of MNP-CA, which achieves stabilization through negatively charged carboxylate groups.

To ascertain how the surface functional groups influence colloidal stability, zeta potential (ζ) measurements were measured for the various MNP samples just after synthesis and as a function of solution pH (Fig. 4). At the synthesis pH (≈6), bare MNPs exhibit a relatively low zeta potential of 10.6 ± 2.00 mV and so they are likely to have limited stability and a tendency toward aggregation, while MNP-APTES and MNP-APTES-GA have zeta potentials of 28.3 ± 1.06 mV and 39.4 ± 1.84 mV, respectively, as shown in Fig. 4a. These results suggest moderate stability for MNP-APTES and strong stability for MNP-APTES-GA, with improved dispersion relative to bare MNPs. As expected, the only MNP sample exhibiting a negative surface charge is MNP-CA, which had a measured zeta potential value of −36.0 ± 1.63 mV. This strong negative zeta potential is consistent with the presence of deprotonated carboxylate functional group,[86] as confirmed by the FTIR analysis, and indicates MNP-CA should exhibit strong stability and effective dispersion in solution.

Understanding this pH-dependent surface charge behavior is critical for identifying conditions under which electrostatic attractions can maximize adsorption performance. The ζ *vs.* pH profiles (Fig. 4b) reveal how the protonation and deprotonation of fixed surface functional groups alter the nanoparticles' net charge across the pH range, shifting their isoelectric points accordingly. The isoelectric point (IEP), defined as the pH at which the particle's net surface charge is zero, corresponding to a zeta potential of 0 mV, provides a critical parameter for understanding colloidal stability. At this point, electrostatic repulsion is minimized, and particles are most prone to agglomeration due to attractive van der Waals forces. For the bare MNPs, the IEP was observed at pH 7.4, consistent with the presence of surface hydroxyl groups that undergo protonation and deprotonation around neutral conditions. Upon modification with APTES, the IEP shifted upward to pH 8.8, which reflects the contribution of protonatable amine groups on the surface; at lower pH, these groups are positively charged, enhancing surface charge density and stability. In contrast, CA functionalization shifted the IEP downward to pH 4.3 due to the abundance of deprotonated carboxylate groups, which impart a strong negative charge to the particle surface in neutral and basic media. For MNP-APTES-GA, the IEP was measured at pH 6.7, an intermediate value that reflects the combined influence of both amine (positively charged at acidic pH) and aldehyde-modified groups with partial negative character. Overall, these shifts do not imply any change in the chemical identity of the grafted moieties but rather reflect how the balance of positively and negatively charged sites evolves across the pH range,

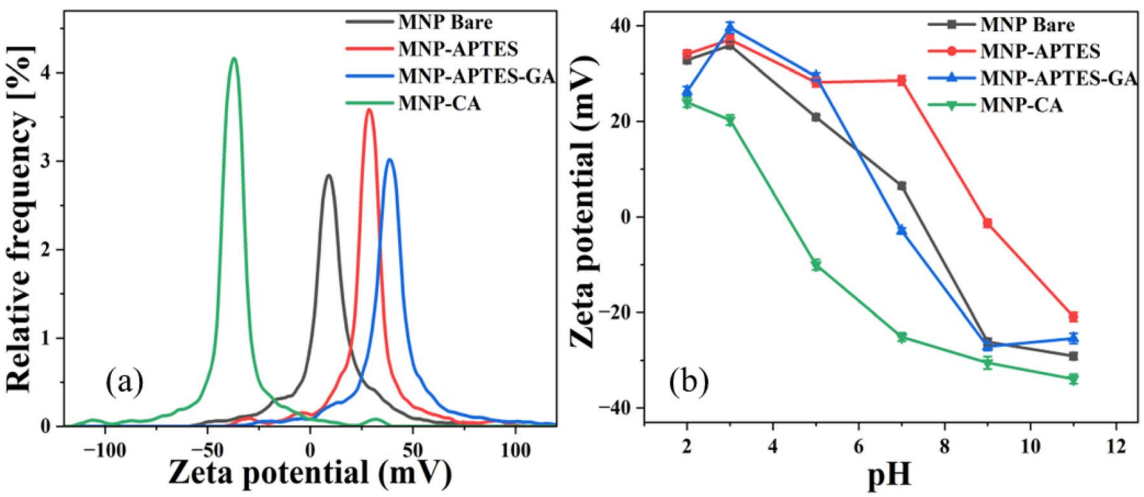

Fig. 4 Zeta potential of MNP samples measured (a) just after synthesis (pH ≈ 6) and (b) at different solution pH values.

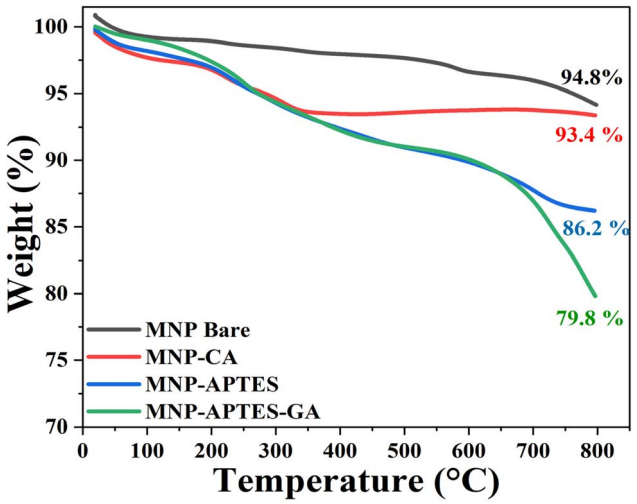

Fig. 5 TGA analysis for the bare MNP and the surface functionalized MNP samples: MNP-APTES; MNP-APTES-GA; and MNP-CA.

enabling precise control over colloidal stability and adsorption interactions in aqueous environments.

To corroborate the formation of coatings on the surface reflected by the deposition of organic and inorganic layers, the thermal stability of bare MNP, MNP-APTES, MNP-APTES-GA, and MNP-CA was studied using thermogravimetric analysis (TGA), as shown in Fig. 5. Upon heating from 0 to 800 °C, bare MNPs exhibited an initial drop of 1.8% between 25 °C and ~150 °C which is attributable to the removal of physiosorbed water. Even up to 800 °C, the weight loss for the bare MNPs was minimal at 5.2%, indicating the inherent thermal stability of unmodified magnetite. In comparison, the functionalized nanoparticles displayed noticeably higher weight losses, consistent with the presence of grafted surface modifiers. A consistent weight decrease was observed between 120 and 150 °C across all samples, due to the removal of adsorbed water and trapped solvents on the surfaces of particles. For MNP-CA, the additional weight loss between 200 and 350 °C is attributed to loss of citric acid.[87,88] MNP-APTES showed additional weight loss between 200–600 °C as the surface-grafted APTES layer decomposed into volatile fragments.[11,30] In the case of MNP-APTES-GA, a more pronounced weight loss above 550 °C was observed, attributable to the combined decomposition of the silane and crosslinked glutaraldehyde networks.[30] The relatively high weight loss recorded for MNP-APTES and MNP-APTES-GA can be attributed to solvent release from the porous, functionalized surfaces and the decomposition of the organic grafted ligands. A similar observation was reported by Ozmen *et al.*,[69] further supporting this interpretation. The grafting ratio can be calculated through the equation:[89]

$$G = \left(1 - \frac{w_1}{w_0}\right) \times 100\% \quad (12)$$

where G is the grafting ratio (wt%), W_1 is the weight percentage of the Fe_3O_4-ligand, and W_0 is the weight percentage of the as-synthesized Fe_3O_4.

Based on the measured weight losses from TGA, the grafting ratio is calculated as 4.6 wt% for CA, 9.1 wt% for APTES, and 7.4 wt% for GA, confirming the successful immobilization of each surface modifier. In the case of the CA-functionalized nanoparticles, the grafting ratio (wt%) was determined from the difference in weight loss between MNP-bare and MNP-CA at 350 °C, the temperature of a distinct mass-loss event observed for MNP-CA, which is attributed to the thermal decomposition of surface-bound citrate moieties.[87,88] The weight loss for MNP-APTES and MNP-APTES-GA was calculated from the overall weight loss difference between these samples and MNP-Bare at 800 °C. Overall, TGA analyses confirm the presence of organic and inorganic ligands on the surface of bare MNP, providing complementary evidence to FTIR and zeta potential analyses. Moreover, while surface functionalization slightly reduces thermal stability due to the introduction of organic coatings, this trade-off is offset by the enhanced surface chemistry, improved colloidal stability, and higher adsorption potential of the functionalized nanoparticles.

SEM analysis was performed to further examine the nanoparticles' morphology, as shown in Fig. 6. While both the bare MNP and MNP-APTES-GA samples showed a strong tendency to agglomerate when dried, this is expected for nanoparticles. SEM images (Fig. 6b) show that MNPs surface-functionalized with APTES and GA largely retain their spherical primary

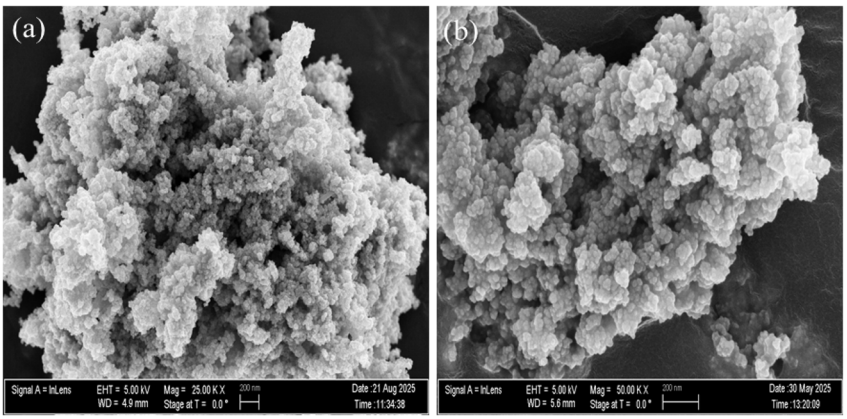

Fig. 6 SEM images of (a) bare MNPs and (b) MNP-APTES-GA.

morphology, but compared to bare MNPs, the functionalized nanoparticles appear slightly larger and form more diffuse aggregates rather than packing tightly into compact clumps. The bare MNPs exhibited an average particle size of 21.25 ± 8.93 nm, while the APTES-GA functionalized MNPs showed an increased average size of 26.09 ± 5.34 nm, consistent with the presence of the surface modification layer. The surface-functionalized MNPs also appeared well-separated, indicating the formation of a consistent shell around each magnetic core. These changes highlight the effectiveness of the functionalization in stabilizing these nanoparticles, making them more suitable for use in broad applications, including wastewater treatment. Reduced agglomeration for the MNP-APTES-GA sample aligns well with the zeta potential results, which demonstrated enhanced colloidal stability due to the introduction of charged surface groups, and with the TGA data, which confirmed the presence of a significant organic surface modification layers through characteristic weight losses. These results are consistent with previous studies by Predescu *et al.*[90] and Mohamed *et al.*[91]

The particle size distribution was examined by TEM, and Fig. 7 presents the data for bare MNPs (as-synthesized) prior to surface modification. TEM analysis reveals that the nanoparticles possess a spherical structure and exhibit a porous texture with a broad distribution. These impurity-free magnetic nanoparticles, characterized by their spherical, porous surfaces, are suitable additives for various applications and can be further functionalized to enhance superparamagnetic properties and mechanical robustness. However, it is important to note that TEM reflects the particles' dry-state morphology. In contrast, DLS had limitations in accurately measuring particles in suspension, often resulting in larger hydrodynamic sizes due to solvation layers, Brownian motion effects, and surface interactions, which can limit the accuracy of size determination in colloidal systems.[92]

DLS confirmed that the optimized co-precipitation method yielded well-dispersed nanoparticle suspensions with relatively narrow size distributions, as shown in Fig. 8a. The average hydrodynamic diameters were 137.33 ± 3.96 nm, 186.23 ± 3.63 nm, 190.90 ± 2.78 nm, and 169.97 ± 2.82 nm for bare MNPs, MNP-APTES, MNP-APTES-GA, and MNP-CA, respectively. The hydrodynamic sizes of the MNPs increased upon surface functionalization due to the presence of grafted organic layers and associated solvation shells. Notably, the value for MNP-CA was 169.97 ± 2.82 nm, a slightly smaller hydrodynamic size than that of the other functionalized MNPs, likely due to the stabilizing influence of CA under optimized synthesis conditions, resulting in a narrow size distribution and reduced

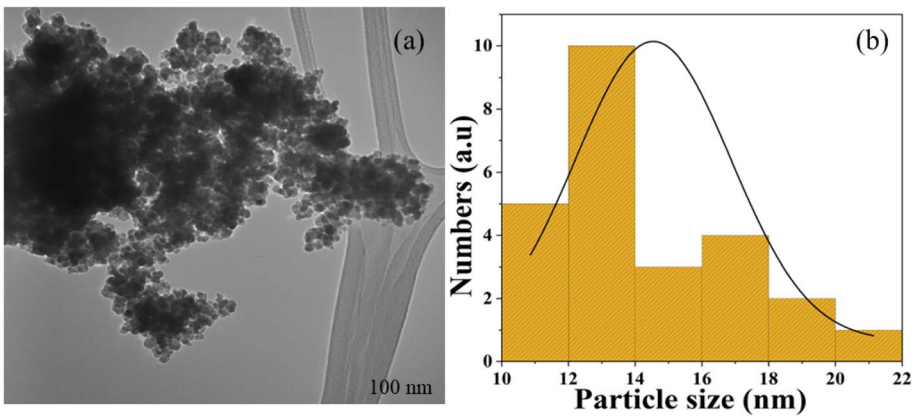

Fig. 7 (a) TEM micrograph of bare magnetic nanoparticles (MNP) and (b) the corresponding particle size distribution.

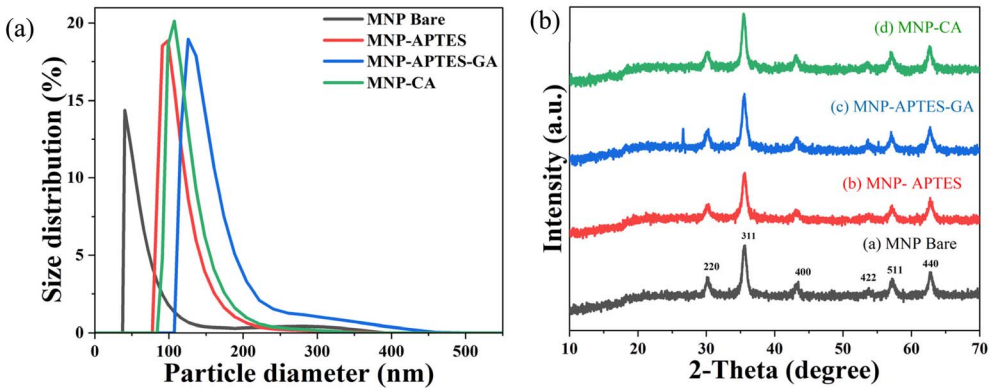

Fig. 8 (a) DLS particle size distribution and (b) X-ray diffractograms of bare MNPs, MNP-APTES, MNP-APTES-GA, and MNP-CA.

aggregation. Similar observations were reported by Sehlleier *et al.*,[93] where surface modification led to a larger hydrodynamic diameter of 237 nm, attributed to the effect of the surface modification of the MNPs.

To verify the crystalline phase and assess the structural stability of the nanoparticles after surface functionalization, X-ray diffraction (XRD) analysis was also performed. Fig. 8b presents the XRD patterns of bare MNPs, MNP-APTES, MNP-APTES-GA, and MNP-CA. All samples exhibit the characteristic diffraction peaks of magnetite (Fe_3O_4) at 2θ values of approximately 30.2° (220), 35.6° (311), 43.3° (400), 53.5° (422), 57.2° (511), and 62.8° (440), confirming the formation of a crystalline cubic spinel structure consistent with the JCPDS card no. 19-0629. The most intense peak was observed at 35.6° (311 plane), which is typical of magnetite and further validates the nanoparticles' crystalline nature. Importantly, no additional diffraction peaks corresponding to other iron oxide phases, such as maghemite (γ-Fe_2O_3) or hematite (α-Fe_2O_3), were detected, indicating that the crystalline structure of magnetite remained intact during surface modification. Using the Scherrer equation, the average size of MNP crystallites was estimated to be 7.67 nm. This crystal size matches other literature where the average MNP crystallite sizes obtained were 7.80 nm,[84] 7.66 nm,[94] 8.31 nm,[95] and 12.0 nm.[63] Moreover, the XRD analysis indicated that the functionalized samples (MNP-APTES, MNP-APTES-GA, and MNP-CA) show no discernible shift in peak positions, though a slight reduction in peak intensity and broadening is noticeable. These effects can be attributed to the presence of organic ligands on the MNP surface for the functionalized samples, which can slightly attenuate the diffraction signal and marginally reduce the apparent crystallinity signal without altering the core spinel phase.

3.2 Adsorption experiments

3.2.1 Effect of contact time. The effect of contact time on Cu^{2+} and MO adsorption by each nano-adsorbent is presented in Fig. 9. In both cases, a rapid initial adsorption was observed due to the abundance of available active sites on the nanoparticle surfaces. With increasing contact time, the adsorption rates gradually slowed and eventually approached equilibrium as the adsorptive sites became progressively occupied and the concentration of adsorbates in solutions decreased.[69,96]

For Cu^{2+} adsorption (Fig. 9a), MNP-APTES-GA exhibited the highest removal efficiency (~18%), followed by MNP-APTES (~13%) and MNP-CA (~11%), while bare MNPs achieved the lowest removal efficiency (~8%). The removal efficiency of Cu^{2+} by bare MNPs, MNP-APTES, and MNP-APTES-GA increased gradually and reached equilibrium at 180 min, indicating saturation of the available active sites, On the other hand, MNP-CA showed a steady increase in Cu^{2+} removal until 150 min, after which equilibrium was attained. This clearly showed that the active sites were exhausted, causing no further adsorption of the Cu^{2+} ions.

In contrast, MO adsorption (Fig. 9b) showed a different performance order, with MNP-APTES-GA again demonstrating the highest efficiency (~74%), followed by MNP-APTES (~62%) and bare MNPs (~47%), whereas MNP-CA displayed only negligible adsorption (~3%). The adsorption of MO by bare MNPs, MNP-APTES, and MNP-APTES-GA increased steadily from 15 to 60 min and reached equilibrium at 90 min. These differences can be attributed to the distinct chemical functionalities introduced during surface modification, which alter the affinity of the nanoparticles toward different classes of pollutants. The superior uptake of Cu^{2+} by amine-functionalized nanoparticles is primarily due to the strong coordination ability of amine groups with metal ions, while the enhanced adsorption of MO is driven by electrostatic interactions between the negatively charged dye molecules and the functional groups present on the nanoparticle surface. Recently, Tziro and Baseri[51] synthesized MNPs by co-precipitation and surface coated them with citric acid, ascorbic acid, salicylic acid, starch, and saccharose. The removal efficiency for Pb^{2+} increased steadily until it reached the equilibrium stage state of dynamic equilibrium,[97] defined as the needed contact time required for adsorption and desorption rates to balance. Similarly, Jayalakshmi *et al.* reported that the adsorption of heavy metals (Pb^{2+} and Zn^{2+}) and dyes (Congo red and methylene green) followed a similar pattern, characterized by rapid uptake at the beginning and a steady increase to equilibrium.[98] In this study, optimization of factors such as

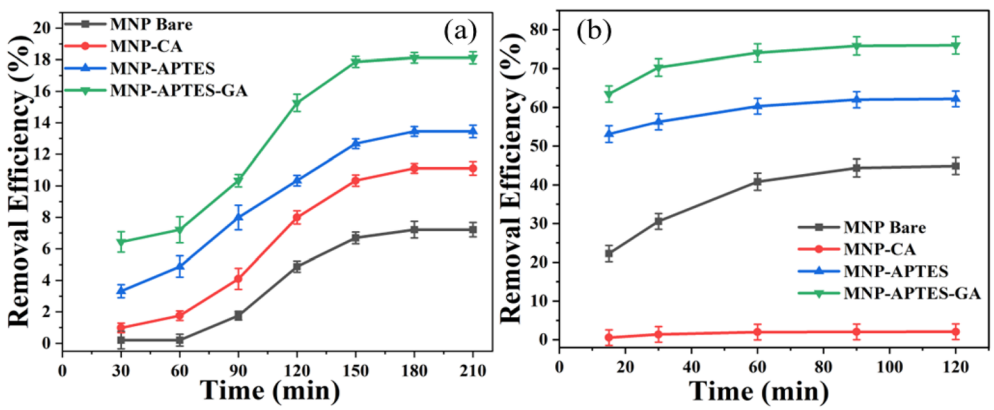

Fig. 9 Effect of contact time on the adsorption efficiency of (a) Cu^{2+} removal at an adsorbent dose of 5 g L^{-1}, initial Cu^{2+} concentration of 500 mg L^{-1} at 25 °C and (b) methyl orange removal at an adsorbent dose of 2 g L^{-1}, initial dye concentration of 45.8 mg L^{-1} at 25 °C.

initial concentration, pH, and adsorbent dose further confirmed that both equilibrium time and adsorption capacity depend strongly on the type of surface modification and the pollutant class being targeted.

3.2.2 Influence of adsorbent dose and initial concentration of Cu^{2+}. The amount of adsorbent and its concentration are crucial factors that govern the overall adsorption capacity. Dosage response experiments were conducted exclusively on the MNP-APTES-GA sorbent because preliminary screening of the synthesized adsorbents had already identified it as the top performer in both adsorption capacity and reproducible dose-dependent responsiveness across contact times. As shown in Fig. 10a, the Cu^{2+} removal efficiency increased from 16.7% to 24% as the MNP-APTES-GA dose was increased. This result is due to the increased number of available adsorption sites at higher MNP-APTES-GA dosages, which facilitates more effective binding of metal ions. The dual APTES-GA functionalization produced a substantially higher density of surface binding sites and markedly improved colloidal stability; together these properties yielded the clearest and most practically relevant dose–efficiency relationship. This adsorbent was selected for a more intensive dosage study with a more detailed evaluation under multiple operating conditions. Mechanistically, the enhanced Cu^{2+} uptake by MNP-APTES-GA likely arises from improved dispersion and surface exposure combined with an increased abundance of functional groups introduced during the modification, which can coordinate with Cu^{2+}. In particular, surface amine groups from APTES and oxygen-containing functionalities from glutaraldehyde are expected to act as coordination sites for Cu^{2+} through lone-pair donation. Such behavior is in good agreement with previous research on nanoparticle-based adsorbents.[81,98–100] The removal efficiency was constant, and Cu^{2+} removal steadily increased slightly at 12.5 g L^{-1} compared to other doses. However, beyond an adsorbent dosage of 15 g L^{-1}, the removal efficiency reached a plateau, which can be attributed to particle agglomeration at higher dosages, reduced dispersion, and possible overlap of active sites. These factors lower the effective surface area available for adsorption. Considering both efficiency and material economy, an optimal adsorbent dose of 12.5 g L^{-1} was selected for subsequent experiments.

There was a noticeable decrease in the removal efficiency of Cu^{2+} as the initial concentration of metal ions increased, as shown in Fig. 10b. This is because the adsorption sites are limited for a given adsorbent dose. For instance, the removal efficiency increased from 22% to 38% when the initial Cu^{2+} concentration decreased from 500 to 100 mg L^{-1}. This was also confirmed in the study by Azzam *et al.*, who reported similar behavior for Ni^{2+}, Cu^{2+}, Cd^{2+}, and Pb^{2+} ions.[101,102] The percentage of Cu^{2+} removal increases from 22 to 38% with a decrease in initial Cu^{2+} concentration from 500–100 mg L^{-1}. The higher removal efficiencies at lower initial concentrations can be explained by the increasing driving force of the Cu^{2+} ions towards the adsorptive or active sites on the MNP-APTES-GA surface coupled with a higher adsorbate-to-site accessibility ratio. At elevated concentrations, the limited number of adsorption sites becomes saturated, leading to reduced percentage removal, even though the absolute amount of adsorbed metal increases. To ensure both practical relevance and analytical reliability, the range of 100–500 mg L^{-1} initial Cu^{2+} concentrations was restricted. This interval mirrors the typical pollutant load encountered in industrial effluents such as metal plating wastewater, while also aligning with the linear calibration range of the UV-vis assay. By doing so, the selected concentration window not only represents realistic environmental conditions but also guarantees sensitivity and accuracy in the measurement of Cu^{2+} removal.

3.2.3. Effect of pH. During adsorption studies, solution pH is another crucial factor that influences the removal efficiency by altering the surface charge of the adsorbent.[103] MNP-APTES-GA was selected as the adsorbent due to its multifunctional surface, featuring both amine and imine groups, which provide strong binding for Cu^{2+} ions and electrostatic interactions with anionic dyes, enabling efficient removal of coexisting pollutants. Additionally, the Fe_3O_4 magnetic core offers high surface area, easy magnetic separation, and reusability, making it suitable for practical wastewater treatment.

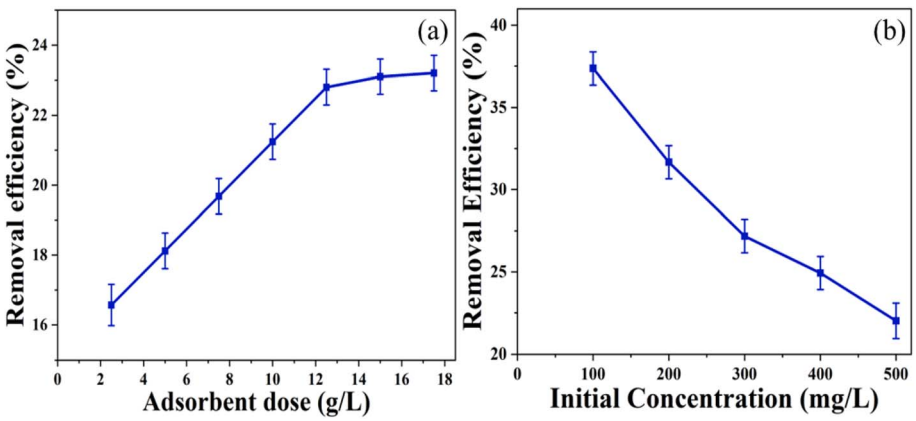

Fig. 10 (a) Removal efficiency of Cu^{2+} with different adsorbent doses of MNP-APTES-GA using an initial Cu^{2+} concentration of 100 mg L^{-1}. (b) With increasing initial Cu^{2+} concentrations, removal efficiencies decreased for the MNP-APTES-GA adsorbent (12.5 g L^{-1} dose). Adsorption studies were conducted at 25 °C with a 180 min contact time.

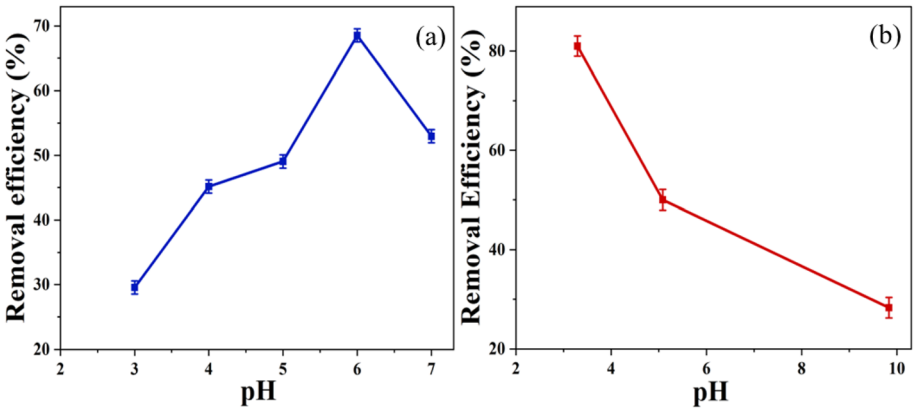

Fig. 11 Effect of solution pH on the adsorption efficiency of MNP-APTES-GA on (a) Cu^{2+} removal at an adsorbent dose of 12.5 g L^{-1} and initial Cu^{2+} concentration of 100 mg L^{-1} (25 °C and 180 min contact time) and (b) MO removal at an initial dye concentration of 45.8 mg L^{-1} and adsorbent dose of 2 g L^{-1} (25 °C and 90 min contact time).

The pH sensitivity of MNP-APTES-GA was evaluated for the adsorption of Cu^{2+} ion and MO. As shown in Fig. 11a, Cu^{2+} removal efficiency increased with rising pH, reaching a maximum of 69% at pH 6 for an initial concentration of 100 mg L^{-1}, after which it declined. In contrast, MO adsorption exhibited its maximum removal efficiency of 83% at pH 3, as illustrated in Fig. 11b. This pH is considered as the operating pH for further experiments. Interestingly, post-adsorption measurements revealed slight shifts in solution pH toward neutrality, indicating buffering tendencies during MO adsorption. These opposite trends can be explained by changes in surface protonation of the MNP-APTES-GA. At low pH, nitrogen-containing groups introduced during APTES-GA functionalization, including imine (–CH═N–) linkages, are expected to undergo protonation to form –CH═NH^+ species, thereby imparting a net positively charged surface.[63] This protonation causes electrostatic repulsion toward Cu^{2+} ions, reducing metal adsorption, while simultaneously enhancing electrostatic attraction toward the negatively charged sulfonate group ($-SO_3^-$) of MO, resulting in higher dye uptake. Conversely, at higher pH values, decreased protonation favors the neutral imine groups for Cu^{2+} adsorption, enhancing metal adsorption but weakening interactions with MO. These complementary adsorption trends underscore the importance of pH in tuning the selectivity of MNP-APTES-GA for coexisting pollutants.

Although iron oxide nanoparticles are susceptible to partial dissolution under strongly acidic conditions due to proton-assisted Fe–O bond cleavage,[104] the APTES-GA surface modification provides a protective organic layer that improves resistance to acid-induced aggregation and surface degradation. Within the operational pH range (~3–10) of this study, no observable loss of magnetic responsiveness, structural integrity, or adsorption performance was detected unlike prior studies.[69] Furthermore, regeneration experiments demonstrated acceptable stability over multiple adsorption–desorption cycles. While very strong acidic conditions (pH < 3) may potentially lead to gradual iron leaching, such conditions are generally outside the typical operational range for wastewater treatment processes. Overall, the functionalized MNP-APTES-GA adsorbent demonstrates adequate chemical stability under the relevant experimental conditions.

3.2.4. Influence of co-existing heavy metals. Wastewater often contains multiple cations, which can potentially affect the adsorption performance of Cu^{2+} ions by competing for active sites on the adsorbent surface. To evaluate the selectivity of the adsorbent towards Cu^{2+}, competitive adsorption experiments were conducted in the presence of additional heavy metals cobalt (Co^{2+}), nickel (Ni^{2+}), zinc (Zn^{2+}), and aluminium (Al^{3+}). These cations can interact with the functional imine and amine groups on the nanoparticle surface, potentially reducing the number of sites available for Cu^{2+} binding. As shown in Fig. 12, Cu^{2+} adsorption decreased in the presence of competing cations compared to the single-metal system, indicating that some competition for active sites occurred. At initial cation concentrations of 125 mg L^{-1}, contact time of 180 min, and adsorbent dose of 10 g L^{-1}, the adsorption of Cu^{2+} in the presence of co-existing heavy metals using MNP-APTES-GA ranged from 22% to 37% in multicomponent solutions, lower than the 53%

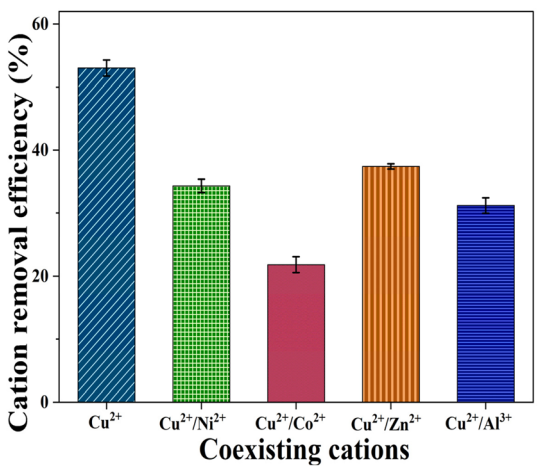

Fig. 12 Effect of co-existing metal ions (Co^{2+}, Ni^{2+}, Zn^{2+}, and Al^{3+}) on the selective adsorption of Cu^{2+} by MNP-APTES-GA particles.

recorded in solutions containing only Cu^{2+}. Among the tested ions, Co^{2+} exhibited the strongest competitive effect, whereas Ni^{2+} and Zn^{2+} caused comparatively smaller reductions in Cu^{2+} adsorption. This decrease in removal efficiency can be attributed to the partial occupation of active imine binding sites by coexisting metal ions. Nevertheless, MNP-APTES-GA exhibited preferential uptake of Cu^{2+} under multicomponent conditions, indicating a relatively higher affinity of the functionalized surface for Cu^{2+} even in the presence of competing cations. While some ions, such as Zn^{2+}, showed partial adsorption onto the nano-adsorbents, the competition for active sites varied depending on ionic charge, molecular mass, hydrated radius, and hydration energy.[105] These results suggest a multi-surface adsorption mechanism, where several functional groups contribute to metal binding and co-existing cations partially interact with the adsorbent without fully displacing Cu^{2+} ions.[106]

The selective adsorption of Cu^{2+} can be explained by the coordination interactions between Cu^{2+} ions and the nitrogen-containing functional groups introduced during APTES-GA modification. The imine (–C=N–) and residual amine ($–NH_2$) functionalities introduced through APTES-GA modification act as electron-donating ligands capable of forming surface coordination complexes with Cu^{2+} *via* lone-pair donation. Compared with competing divalent cations, Cu^{2+} exhibits stronger complexation affinity toward nitrogen-containing ligands due to its favorable distortion and higher ligand-field stabilization energy. These factors promote preferential surface complexation, consistent with recent reports highlighting the importance of specific coordination environments in driving selective heavy-metal adsorption in mixed-ion systems.[107,108] In addition to metal-ion adsorption, the adsorbent also demonstrated effective removal of MO through a different adsorption mechanism. Selective adsorption under acidic conditions is primarily governed by electrostatic attraction and supramolecular interactions. At low pH, protonation of imine groups generates positively charged surface sites (–CH=NH^+), enhancing electrostatic interaction with the anionic sulfonate ($–SO_3^-$) groups of MO. Furthermore, hydrogen bonding and other interactions between aromatic moieties of MO and surface functionalities contribute to chemisorption behavior, as confirmed by FTIR spectral shifts after adsorption. Unlike Cu^{2+}, which possibly relies on coordination interactions, MO adsorption proceeds through multimodal interactions involving electrostatic attraction, hydrogen bonding, and van der Waals forces, leading to heterogeneous multilayer adsorption.[109] Overall, the high selectivity observed in complex systems is not governed by a single interaction mechanism but rather by the synergistic interplay of surface complexation, electrostatic forces, and supramolecular interactions. Although, Cu^{2+} and MO adsorption were evaluated independently under their respective optimized conditions, the multifunctional surface chemistry of MNP-APTES-GA enables effective removal of both heavy metal ions and anionic dyes, highlighting its strong potential for application in multi-contaminant wastewater systems.

3.2.5 Desorption and reusability of the adsorbent. The reusability of an adsorbent is critical in its practical application for wastewater treatment, as it determines both cost-effectiveness and long-term stability. In this work, the regeneration of MNP-APTES-GA was assessed over five adsorption–desorption cycles using NaOH for MO and HCl for Cu^{2+}. Fig. 13a and b illustrates the desorption efficiency of MO and Cu^{2+} ions from MNP-APTES-GA over five consecutive adsorption–desorption cycles. In the first cycle, MO desorption efficiency was about ~91%, which confirms the effectiveness of NaOH as an eluent in releasing MO molecules from the adsorbent surface. In the second and third cycles, the efficiency decreased only slightly to ~89% and ~87%, respectively, indicating that the adsorbent maintained most of its regeneration capacity during repeated use. A more pronounced decline was observed in the fourth (~85%) and fifth (~80%) cycles, which could be associated with the gradual deactivation of active sites or minor structural changes to the surface functional groups after repeated exposure to alkaline conditions. Despite a gradual decline in performance, the desorption efficiency remained above 80% after five cycles, suggesting that MNP-APTES-GA retains a high level of stability and can be reused multiple

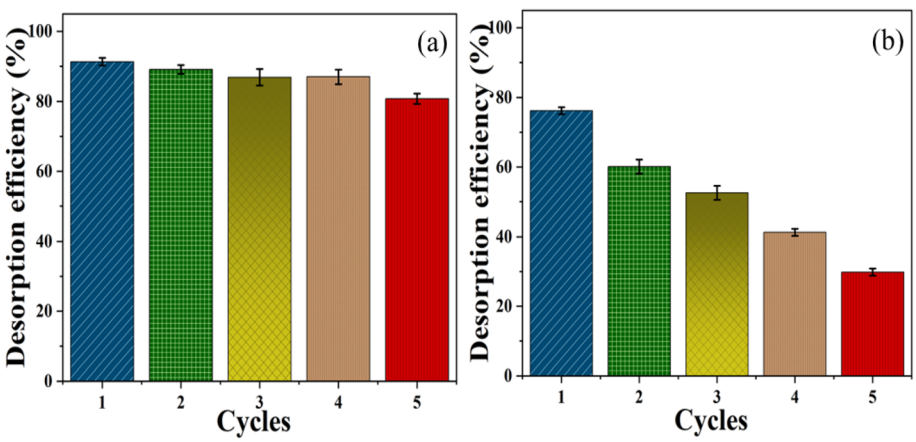

Fig. 13 Contrasting desorption and reusability behavior of MNP-APTES-GA showing effective regeneration for (a) MO and limited regeneration for (b) Cu^{2+}.

times with minimal performance loss. The gradual decline is likely due to partial occupation or blockage of imine functional groups, irreversible binding of dye molecules, or a combination of electrostatic interaction, complexation, and physical adsorption mechanisms that prevent complete desorption in successive cycles.[57]

In contrast, Cu^{2+} desorption (Fig. 13b) began at ~76% when HCl was used as the eluent, indicating that acid effectively disrupts Cu^{2+}–imine coordination bonds. However, unlike MO desorption, a sharper decline in efficiency was observed over successive cycles. After the second and third cycles, the desorption efficiency decreased to ~62% and ~52%, respectively, while a substantial reduction to ~30% was recorded in the fifth cycle. The stronger decline can be attributed to the formation of stable coordination complexes with imine groups and potential adsorbent degradation under acidic conditions, as supported by the observed ~15% material loss after repeated acid exposure. Although the adsorbent retained some reusability for Cu^{2+}, these results suggest that its long-term regeneration efficiency is limited under acidic conditions and optimization of desorption conditions would be necessary for improved recovery. The findings of this reusability study highlight that while MNP-APTES-GA demonstrates excellent durability and regeneration efficiency for MO dye removal, its performance in repeated Cu^{2+} desorption cycles could stand to be improved through the development of more suitable eluents or milder regeneration conditions.

3.3 Adsorption kinetics

Adsorption kinetic studies were performed to examine the relationship between adsorption capacity and time, providing insights into adsorption rates and equilibrium mechanisms.[79] The pseudo-first-order model generally describes physisorption, while the pseudo-second-order model often represents chemisorption processes. In this study, the kinetic modelling results revealed distinct behaviors for Cu^{2+} and MO adsorption on MNP-APTES-GA as shown in Fig. 14 and 15 and Table 2. For Cu^{2+} adsorption, the correlation coefficient ($R^2 = 0.8885$) was higher for the pseudo-first-order model compared to the pseudo-second-order model ($R^2 = 0.8091$), indicating that the adsorption process is better described by the pseudo-first-order

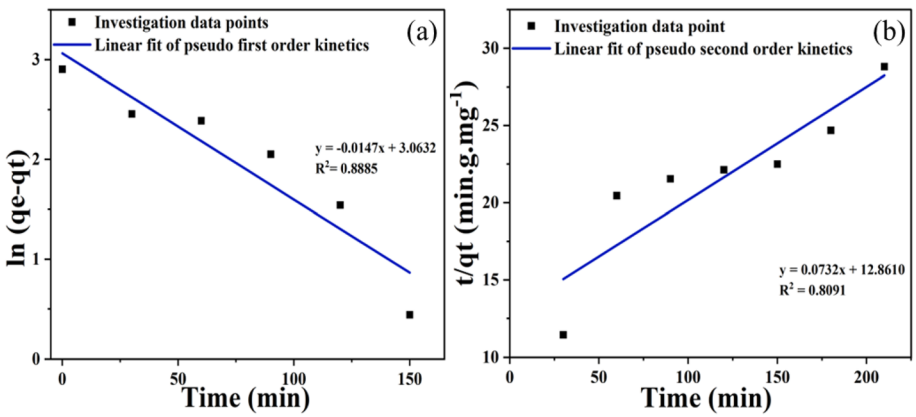

Fig. 14 Kinetic modelling of Cu^{2+} adsorption onto MNP-APTES-GA: (a) pseudo-first-order kinetics and (b) pseudo-second-order kinetics. Experimental data were fitted to assess the adsorption mechanism and rate-limiting steps.

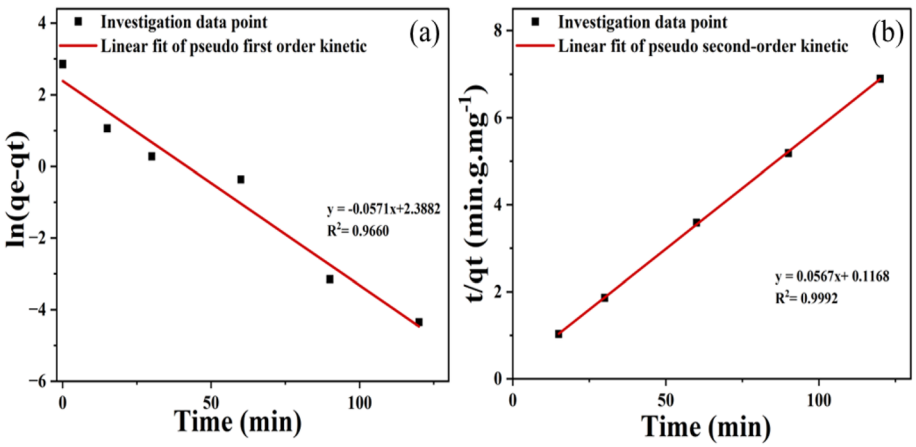

Fig. 15 Kinetic modelling of methyl orange adsorption onto MNP-APTES-GA: (a) pseudo-first-order kinetics and (b) pseudo-second-order kinetics. Experimental data were fitted to assess the adsorption mechanism and rate-limiting steps.

Table 2 Estimated kinetic constants of pseudo-first-order and pseudo-second-order for Cu^{2+} and methyl orange adsorption by MNP-APTES-GA

	Pseudo-first-order model			Pseudo-second-order model		
Adsorbate	R^2	K_1 (min^{-1})	q_e (mg g^{-1})	R^2	K_2 (g mg^{-1} min^{-1})	q_e (mg g^{-1})
Cu^{2+}	0.8885	0.0147	21.390	0.8091	1.6×10^{-4}	34.132
MO	0.9660	0.0571	10.891	0.9992	0.0151	17.951

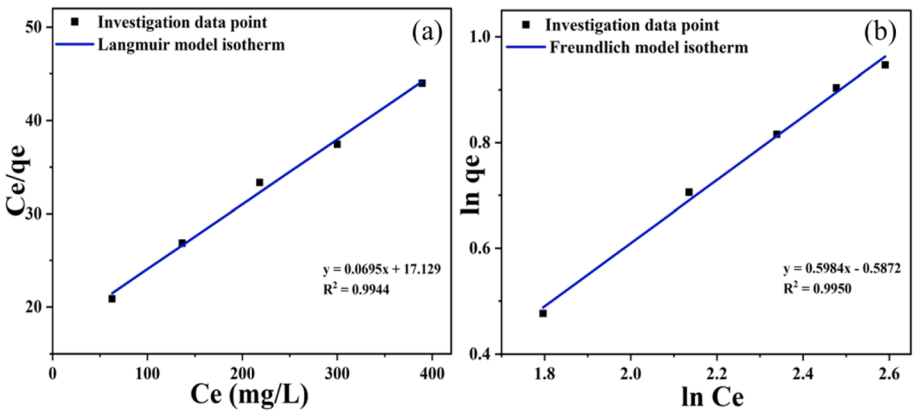

Fig. 16 Isotherm modeling of Cu^{2+} adsorption onto the MNP-APTES-GA: (a) Langmuir isotherm model and (b) Freundlich isotherm model. The models were applied to evaluate adsorption capacity and surface interaction behavior.

kinetics. This suggests that Cu^{2+} adsorption is dominated by physisorption mechanisms rather than strong chemical bonding. Moreover, the theoretical adsorption capacity (q_e, cal) of 18.23 mg g^{-1} closely matched the experimental value (q_e, exp) of 21.39 mg g^{-1} for the pseudo-first-order model, further supporting the applicability of this kinetic model for the Cu^{2+} adsorption process.

In contrast, MO adsorption was better fitted by the pseudo-second-order model, with a correlation coefficient (R^2 = 0.9992) that was higher than that of the pseudo-first-order model (R^2 = 0.9660). The good agreement between the calculated and experimental q_e values in the pseudo-second-order model indicates that MO adsorption tends toward chemisorption. The correlation coefficient is closer to unity for the pseudo-second order than the first-order model, which also indicates that their adsorption tends to be chemisorption held on by chemical bonds. This process is likely governed by electrostatic attraction between the positively charged surface functional groups of MNP-APTES-GA and the negatively charged dye molecules, as also reported in a similar study by Muthukumaran *et al.*[81] Overall, these results demonstrate that Cu^{2+} adsorption on MNP-APTES-GA primarily follows physisorption, whereas MO adsorption is dominated by chemisorption, highlighting the dual adsorption mechanisms enabled by the multifunctional surface chemistry of the adsorbent.

3.4 Adsorption isotherms

From the adsorption isotherm models, it is evident that there is a direct relationship between the initial Cu^{2+} concentration and adsorption capacity. Fig. 16 illustrates the impact of the initial concentration on Cu^{2+}, the uptake, and the corresponding Langmuir and Freundlich isotherms, while the estimated parameters for the isotherm are summarized in Table 3.

The correlation coefficients (R^2) for the Langmuir and Freundlich models are 0.9944 and 0.9950, respectively, indicating that both models provide an excellent fit to the experimental data, with the Freundlich model showing slightly better linearity (Fig. 16). This suggests that Cu^{2+} adsorption onto MNP-APTES-GA can occur through both monolayer adsorption on a homogeneous surface (Langmuir) and multilayer adsorption on a heterogeneous surface (Freundlich). Additionally, the dimensionless separation factor R_L, which characterizes the favorability of Langmuir-type adsorption, was calculated to range from 0.71 to 0.33 for initial Cu^{2+} concentrations between 100 and 500 mg L^{-1}. In general, $R_L > 1$ denotes unfavorable adsorption, $R_L = 1$ suggests linear adsorption, $0 < R_L < 1$ indicates favorable adsorption, and $R_L = 0$ signifies irreversible adsorption. Since all calculated values fall between 0 and 1, the adsorption of Cu^{2+} onto MNP-APTES-GA is confirmed to be

Table 3 Estimated adsorption isotherm parameters for the Langmuir and Freundlich isotherm models for Cu^{2+} adsorption by MNP-APTES-GA

	Langmuir isotherm			Freundlich isotherm		
Metal	R^2	K_1 (L mg^1)	Q_m (mg g^{-1})	R^2	K_f (L mg^{-1})	n
Cu^{2+}	0.9944	0.0041	14.390	0.9950	0.2587	1.6710

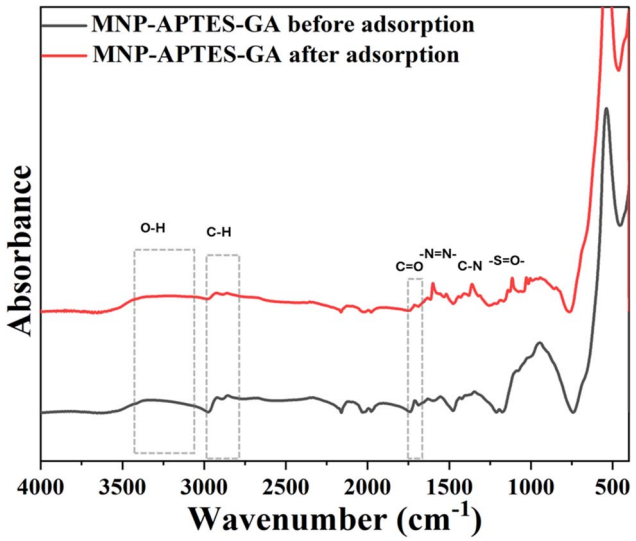

Fig. 17 FTIR spectra of MNP-APTES-GA before and after methyl orange adsorption.

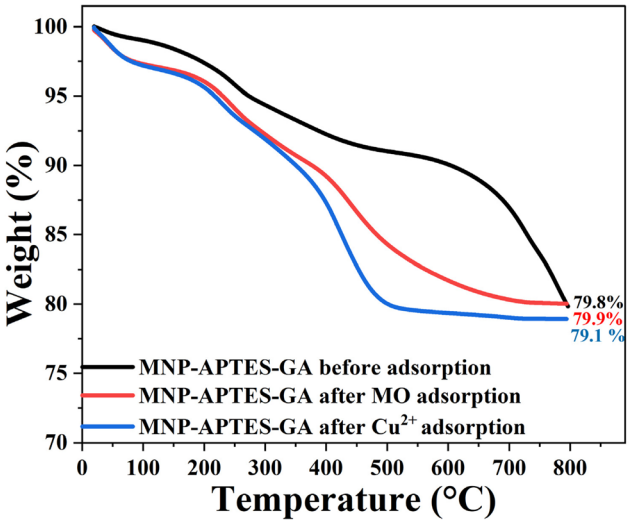

Fig. 18 TGA of MNP-APTES-GA before and after MO and Cu^{2+} adsorption.

favorable. The adsorption mechanism of MO was further elucidated through FTIR analysis, as shown in Fig. 17 and Table 4. After adsorption, a decrease in the O–H band suggested hydrogen bonding between surface hydroxyl groups and dye molecules. A decrease in intensity and shift in stretching vibration of –C=O from 1709 to 1695 cm^{-1} and changes in Si–O–Si bands attest to their participation in the adsorption process. Additionally, the appearance of new sharp peaks at 1595 cm^{-1} (–N=N– stretching), 1275 cm^{-1} (C–N stretching), and 1144 cm^{-1} (S=O stretching of sulfonic groups), indicates the successful anchoring of the azo dye on the sorbent surface.[110–112]

After five adsorption–desorption cycles, TGA was again performed to evaluate the structural stability of the adsorbent. After adsorption of MO and Cu^{2+}, the overall thermal decomposition profiles remained largely comparable to that of the material, indicating that the functionalized coating remained structurally intact during the adsorption process after 5 cycles, as shown in Fig. 18. The residual weights at 800 °C were 79.8% for the initial adsorbent used, 79.9% after MO adsorption, and 79.1% after Cu^{2+} adsorption, suggesting only minor variation in the organic content of the material. These results confirm that the grafted organic layer remains stable after adsorption and that no significant degradation of the functionalized surface occurs during the adsorption process to the adsorbent. To further examine changes in surface charge following adsorption, zeta potential measurements were performed. The pristine MNP-APTES-GA exhibited a zeta potential value of 39.4 ± 1.84 mV, indicating a highly charged surface resulting from the protonated groups. After adsorption, the zeta potential decreased to 20.1 ± 2.60 mV for Cu^{2+} and 1.40 ± 1.21 mV for MO adsorption respectively, reflecting the interaction of the adsorbates with the active surface sites. The decrease in surface charge suggests partial occupation or neutralization of surface functional groups during adsorption while still maintaining surface stability.[116] These observations support the proposed adsorption mechanism and confirm the structural stability of the adsorbent during the adsorption process.

It is important to note that the adsorption behavior differs between Cu^{2+} and MO due to the distinct nature of the adsorbates. Cu^{2+} ions are small, hydrated cations that predominantly undergo electrostatic attraction and surface complexation with negatively charged or electron-donating groups, resulting in monolayer adsorption consistent with the Langmuir model. In contrast, MO is a larger aromatic azo dye bearing sulfonic and azo functional groups, which interact *via* multiple mechanisms, including electrostatic attraction, hydrogen bonding, van der Waals forces, and π–π interactions. FTIR evidence confirms the active participation of these groups, leading to a more complex and heterogeneous adsorption process. Despite these

Table 4 Functional groups reported in the literature for methyl orange, including key absorbances

Dye structure	Key functional groups	Wavenumbers (cm^{-1})	References
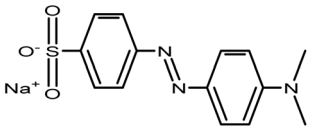	Sulfonate group ($-SO_3^-$)	1000–1200 cm^{-1}	Extremera *et al.*,[112] Imene *et al.*,[113] Wang *et al.*[114]
	Azo linkage (–N=N–)	1594, 1605 cm^{-1}	Bozbay *et al.*,[115] Wang *et al.*[114]
	Aromatic rings	700–1500 cm^{-1}	Extremera *et al.*,[112] Imene *et al.*,[113] Bozbay *et al.*[115]
	C–N	1278 cm^{-1}	Extremera *et al.*[112]

differences in adsorption mechanisms and kinetics—Cu^{2+} following pseudo-first-order and MO following pseudo-second-order kinetics—the multifunctional surface chemistry of MNP-APTES-GA enables effective removal of both contaminants. Furthermore, the minimal changes observed in TGA profiles and zeta potential after adsorption confirm the structural stability and sustained activity of the adsorbent. Even though the adsorption kinetics differ among pollutants, this combination of dual functionality, stability, and reusability underscores the advantages of the present system over conventional single-pollutant adsorbents and highlights its potential for practical wastewater treatment applications.

4 Conclusions

This study demonstrates that magnetic nanoparticles can be efficiently synthesized *via* a simple chemical co-precipitation route and subsequently functionalized with 3-aminopropyltriethoxysilane, glutaraldehyde, and citric acid. Comprehensive characterization confirmed the successful attachment of each ligand without compromising the intrinsic magnetic properties of the nanoparticle core, while also revealing that dual silane-crosslinker modification of MNP-APTES-GA significantly enhances superior colloidal stability and dispersion compared to single-ligand systems. When evaluated for pollutant uptake, MNP-APTES-GA consistently outperformed bare MNP, MNP-CA, and MNP-APTES, achieving up to ~69% Cu^{2+} removal at pH 6 under optimized contact time, adsorbent dose, initial concentration, and competing ions conditions, and ~83% methyl orange removal at pH 3. These outcomes firmly establish its dual functionality toward simultaneous remediation of heavy metals and anionic organic dyes. Kinetic analyses demonstrated that Cu^{2+} adsorption follows a pseudo-first-order mechanism, whereas methyl orange conforms to a pseudo-second-order model. Equilibrium data for Cu^{2+} adsorption fit both Langmuir and Freundlich isotherms, indicating a hybrid monolayer-heterogeneous sorption processes. Importantly, in multicomponent wastewater containing Co^{2+}, Ni^{2+}, Zn^{2+}, and Al^{3+}, MNP-APTES-GA adsorbent exhibited a strong preferential affinity toward Cu^{2+}, suggesting a multi-surface adsorption phenomenon rather than simple competitive inhibition. Furthermore, desorption and regeneration studies confirmed that the functionalized nanoparticles retain their moderate to high removal efficiency for both Cu^{2+} (~76–30%) and methyl orange (~91–80%) over five consecutive cycles. Overall, the results position MNP-APTES-GA as a robust, scalable, dual-functional, and recyclable adsorbent with significant promise for advanced water-purification applications.

Conflicts of interest

There are no conflicts to declare.

Data availability

The data supporting this study are available within the article. Additional data are available from the corresponding author upon reasonable request.

Acknowledgements

We appreciate Dr Mourad Benamara and Serhii Kryvyi of the Institute for Nanoscience and Engineering at the University of Arkansas for providing access to TEM instrumentation and XRD data collection and interpretation. We also thank Dr Preston Larson of the Samuel Roberts Noble Microscopy Laboratory at the University of Oklahoma for support with SEM imaging.

References

1 P. N. Dave and L. V. Chopda, *J. Nanotechnol.*, 2014, **2014**(1), 398569.
2 R. Bhateria and R. Singh, *J. Water Proc. Eng.*, 2019, **31**, 100845.
3 K. Thirumoorthy and S. Krishna, *J. Environ. Chem. Eng.*, 2020, **8**, 103582.
4 V. K. Gupta, A. Rastogi and A. Nayak, *J. Colloid Interface Sci.*, 2010, **342**, 135–141.
5 E. Iakovleva and M. Sillanpää, *Environ. Sci. Pollut. Res.*, 2013, **20**, 7878–7899.
6 M. Chalaris, D. A. Gkika, A. K. Tolkou and G. Z. Kyzas, *Environ. Sci. Pollut. Res.*, 2023, **30**, 119627–119653.
7 S. Singh, K. Barick and D. Bahadur, *Nanomater. Nanotechnol.*, 2013, **3**, 20.
8 F. S. A. Khan, N. M. Mubarak, M. Khalid, R. Walvekar, E. C. Abdullah, S. A. Mazari, S. Nizamuddin and R. R. Karri, *Environ. Sci. Pollut. Res.*, 2020, **27**, 24342–24356.
9 P. Saharan, G. R. Chaudhary, S. Mehta and A. Umar, *J. Nanosci. Nanotechnol.*, 2014, **14**, 627–643.
10 S. Jin, B. C. Park, W. S. Ham, L. Pan and Y. K. Kim, *Colloids Surf., A*, 2017, **531**, 133–140.
11 A. Abdolmaleki, S. Mallakpour and S. Borandeh, *RSC Adv.*, 2015, **5**, 90602–90608.
12 A. A. Joshi, K. Chaudhari and G. Ragupathy, *Environ. Sci. Water Res. Technol.*, 2026, (12), 421–456.
13 R. Kandasamy, *Sep. Purif. Technol.*, 2017, **188**, 458–467.
14 A. Masjedi, E. Askarizadeh and S. Baniyaghoob, *Mater. Chem. Phys.*, 2020, **249**, 122917.
15 K. Al-Saad, M. Amr, D. Hadi, R. Arar, M. Al-Sulaiti, T. Abdulmalik, N. Alsahamary and J. Kwak, *Arab. J. Nucl. Sci. Appl.*, 2012, **45**, 335–346.
16 S. Nizamuddin, M. Siddiqui, N. Mubarak, H. A. Baloch, E. Abdullah, S. A. Mazari, G. Griffin, M. Srinivasan and A. Tanksale, *Nanoscale Materials in Water Purification*, 2019, pp. 447–472.
17 F. Almomani, R. Bhosale, M. Khraisheh and T. Almomani, *Appl. Surf. Sci.*, 2020, **506**, 144924.
18 M. Faraji, Y. Yamini and M. Rezaee, *J. Iran. Chem. Soc.*, 2010, **7**, 1–37.
19 X. Zeng, G. Zhang, J. Zhu and Z. Wu, *Environ. Sci. Water Res. Technol.*, 2022, **8**, 907–925.
20 S. R. Chowdhury, E. K. Yanful and A. R. Pratt, *Environ. Earth Sci.*, 2011, **64**, 411–423.
21 A. D. Abid, M. Kanematsu, T. M. Young and I. M. Kennedy, *Aerosol Sci. Technol.*, 2013, **47**, 169–176.

22 J. Zhang, S. Lin, M. Han, Q. Su, L. Xia and Z. Hui, *Water*, 2020, **12**, 446.
23 S. Rajput, C. U. Pittman and D. Mohan, *J. Colloid Interface Sci.*, 2016, **468**, 334–346.
24 P. Yuan, M. Fan, D. Yang, H. He, D. Liu, A. Yuan, J. Zhu and T. Chen, *J. Hazard. Mater.*, 2009, **166**, 821–829.
25 Y. Liu, J. Bai, H. Duan and X. Yin, *Chin. J. Chem. Eng.*, 2017, **25**, 32–36.
26 X. S. Wang, L. Zhu and H. J. Lu, *Desalination*, 2011, **276**, 154–160.
27 Y. Bagbi, A. Sarswat, D. Mohan, A. Pandey and P. R. Solanki, *J. Environ. Chem. Eng.*, 2016, **4**, 4237–4247.
28 P. Chen, M. P. Prange, D. Song, S. Lee, S. S. Lee, J. Liu, Y. Zhao, X. Wang, M. H. Engelhard and Y. Zhou, *Environ. Sci. Technol.*, 2025, **59**, 11862–11874.
29 H. A. Wiatrowski, S. Das, R. Kukkadapu, E. S. Ilton, T. Barkay and N. Yee, *Environ. Sci. Technol.*, 2009, **43**, 5307–5313.
30 V. J. Inglezakis, A. Kurbanova, A. Molkenova, A. A. Zorpas and T. S. Atabaev, *Sustainability*, 2020, **12**, 5489.
31 K. Zargoosh, H. Abedini, A. Abdolmaleki and M. R. Molavian, *Ind. Eng. Chem. Res.*, 2013, **52**, 14944–14954.
32 X. Xin, Q. Wei, J. Yang, L. Yan, R. Feng, G. Chen, B. Du and H. Li, *Chem. Eng. J.*, 2012, **184**, 132–140.
33 D. S. Chaudhari, R. P. Upadhyay, G. Y. Shinde, M. B. Gawande, J. Filip, R. S. Varma and R. Zbořil, *Green Chem.*, 2024, **26**, 7579–7655.
34 Y. Iqbal, W. Ma, X. Li, S. Fu, A. Shahzad, I. Ahmad, Y. Wang, M. Adil and M. Abohashrh, *Water, Air, Soil Pollut.*, 2025, **236**, 687.
35 M. S. Alshammari, M. M. El-Tyieb, M. E. Fawzy, E. S. Al-Farraj and H. M. Ahmed, *PLoS One*, 2025, **20**, e0329686.
36 S. T. Aly, A. Saed, A. Mahmoud, M. Badr, S. S. Garas, S. Yahya and K. H. Hamad, *Sci. Rep.*, 2024, **14**, 20100.
37 B. Rahmanivahid, F. Naderi and H. Nayebzadeh, *J. Water Environ. Nanotechnol.*, 2020, **5**, 1–16.
38 A. Afkhami and R. Moosavi, *J. Hazard. Mater.*, 2010, **174**, 398–403.
39 G. Vochiţa, A. R. Fânaru-Balint, A. Agavriloaei, D. Gherghel, M. Răcuciu and D. Creangă, *Molecules*, 2025, **30**, 4447.
40 D. Xiao, T. Lu, R. Zeng and Y. Bi, *Microchim. Acta*, 2016, **183**, 2655–2675.
41 Y. Wanna, A. Chindaduang, G. Tumcharern, D. Phromyothin, S. Porntheerapat, J. Nukeaw, H. Hofmann and S. Pratontep, *J. Magn. Magn. Mater.*, 2016, **414**, 32–37.
42 B. Paul, V. Parashar and A. Mishra, *Environ. Sci. Water Res. Technol.*, 2015, **1**, 77–83.
43 D. Chen, T. Awut, B. Liu, Y. Ma, T. Wang and I. Nurulla, *e-Polymers*, 2016, **16**, 313–322.
44 K. Turcheniuk, A. V. Tarasevych, V. P. Kukhar, R. Boukherroub and S. Szunerits, *Nanoscale*, 2013, **5**, 10729–10752.
45 B. Natarajan, P. Kannan, J. A. Rather and R. A. Sheikh, *J. Taiwan Inst. Chem. Eng.*, 2023, **147**, 104942.
46 Y. Liu, Y. Li, X.-M. Li and T. He, *Langmuir*, 2013, **29**, 15275–15282.
47 A. L. Campaña, A. Guillén, R. Rivas, V. Akle, J. C. Cruz and J. F. Osma, *Molecules*, 2021, **26**, 4150.
48 A. A. Pawar, R. Kumar, S. Sharma and T. Satyanarayana, *Part. Part. Syst. Char.*, 2022, **39**, 2200156.
49 R. K. Sharma, K. Solanki, R. Dixit, S. Sharma and S. Dutta, *Environ. Sci. Water Res. Technol.*, 2021, **7**, 818–860.
50 D. Singh, R. K. Gautam, R. Kumar, B. K. Shukla, V. Shankar and V. Krishna, *J. Water Proc. Eng.*, 2014, **4**, 233–241.
51 H. Baseri and S. Tizro, *J. Adv. Mater. Process.*, 2016, **4**, 15–29.
52 T.-g. Yan and L.-j. Wang, *Water Sci. Technol.*, 2014, **69**, 612–621.
53 B. E. Keshta and A. H. Gemeay, *J. Hazard. Toxic Radioact. Waste*, 2022, **26**, 04021042.
54 R. Wo, Q.-L. Li, C. Zhu, Y. Zhang, G.-f. Qiao, K.-y. Lei, P. Du and W. Jiang, *J. Chem. Eng. Data*, 2019, **64**, 2455–2463.
55 A. A. Alqadami, M. Naushad, M. A. Abdalla, M. R. Khan and Z. A. Alothman, *J. Chem. Eng. Data*, 2016, **61**, 3806–3813.
56 A. A. Alqadami, M. Naushad, M. A. Abdalla, T. Ahamad, Z. A. Alothman and S. M. Alshehri, *RSC Adv.*, 2016, **6**, 22679–22689.
57 W. Qu, D. He, Y. Guo, Y. Tang, J. Shang, L. Zhou, R. Zhu and R.-J. Song, *Ind. Eng. Chem. Res.*, 2019, **58**, 18508–18518.
58 A. N. Baghani, A. H. Mahvi, M. Gholami, N. Rastkari and M. Delikhoon, *J. Environ. Health Sci. Eng.*, 2016, **14**, 11.
59 J. Shi, H. Li, H. Lu and X. Zhao, *J. Chem. Eng. Data*, 2015, **60**, 2035–2041.
60 Y. Liu, M. Chen and H. Yongmei, *Chem. Eng. J.*, 2013, **218**, 46–54.
61 S. Ghafoor and S. Ata, *J. Chil. Chem. Soc.*, 2017, **62**, 3588–3592.
62 M. Ozmen, K. Can, G. Arslan, A. Tor, Y. Cengeloglu and M. Ersoz, *Desalination*, 2010, **254**, 162–169.
63 V. Kothavale, V. Karade, P. Waifalkar, S. C. Sahoo, P. Patil and P. Patil, *AIP Conf. Proc.*, 2018, **1942**(1), 050038.
64 A. Jangra, J. Singh, J. Kumar, K. Rani, P. Kumar, S. Kumar, D. Singh and R. Kumar, *Biointerface Res. Appl. Chem.*, 2023, **13**, 325.
65 M. Yang, S. Dang, L. Gao and J. Zhang, *Sci. Rep.*, 2026, **14**(1), 11.
66 M. Abedi, M. Ahmadmoazzam and N. Jaafarzadeh, *Chem. Biochem. Eng. Q.*, 2018, **32**, 205–213.
67 F. Hosseini, M. Seyedsadjadi and N. Farhadyar, *Orient. J. Chem.*, 2014, **30**(4), 1609–1618.
68 M. Karimi, S. A. Milani and H. Abolgashemi, *J. Nucl. Mater.*, 2016, **479**, 174–183.
69 M. Ozmen, K. Can, G. Arslan, A. Tor, Y. Cengeloglu and M. Ersoz, *Desalination*, 2010, **254**, 162–169.
70 J. C. Chacón-Torres, C. Reinoso, D. G. Navas-León, S. Briceño and G. González, *Sci. Rep.*, 2020, **10**, 19004.
71 M. A. Dheyab, A. A. Aziz, M. S. Jameel, O. A. Noqta, P. M. Khaniabadi and B. Mehrdel, *Sci. Rep.*, 2020, **10**, 10793.
72 S. K. Panda, I. Aggarwal, H. Kumar, L. Prasad, A. Kumar, A. Sharma, D.-V. N. Vo, D. Van Thuan and V. Mishra, *Environ. Chem. Lett.*, 2021, **19**, 2487–2525.

73 M. Shariati-Rad, M. Irandoust, S. Amri, M. Feyzi and F. Ja'fari, *Int. Nano Lett.*, 2014, **4**, 91–101.
74 A. Afkhami, M. Saber-Tehrani and H. Bagheri, *Desalination*, 2010, **263**, 240–248.
75 S. Sulaiman, R. a. S. Azis, I. Ismail, H. C. Man, K. F. M. Yusof, M. U. Abba and K. K. Katibi, *Nanoscale Res. Lett.*, 2021, **16**, 1–17.
76 J. Bayuo, M. A. Abukari and K. B. Pelig-Ba, *Appl. Water Sci.*, 2020, **10**, 171.
77 M.-W. Wan, C.-C. Kan, B. D. Rogel and M. L. P. Dalida, *Carbohydr. Polym.*, 2010, **80**, 891–899.
78 L. Zhai, Z. Bai, Y. Zhu, B. Wang and W. Luo, *Chin. J. Chem. Eng.*, 2018, **26**, 657–666.
79 X. Wang, C. Jiang, B. Hou, Y. Wang, C. Hao and J. Wu, *Chemosphere*, 2018, **206**, 587–596.
80 S. Singh, D. Kapoor, S. Khasnabis, J. Singh and P. C. Ramamurthy, *Environ. Chem. Lett.*, 2021, **19**, 2351–2381.
81 C. Muthukumaran, V. M. Sivakumar and M. Thirumarimurugan, *J. Taiwan Inst. Chem. Eng.*, 2016, **63**, 354–362.
82 P. Xu, G. M. Zeng, D. L. Huang, C. Lai, M. H. Zhao, Z. Wei, N. J. Li, C. Huang and G. X. Xie, *Chem. Eng. J.*, 2012, **203**, 423–431.
83 J. Chen, L. An, J. W. Heo, J. H. Bae, H. Jeong and Y. S. Kim, *J. Wood Chem. Technol.*, 2022, **42**, 114–124.
84 B. Malaikozhundan, R. Krishnamoorthi, J. Vinodhini, K. S. N. Nambi and S. Palanisamy, *Inorg. Chem. Commun.*, 2022, **144**, 109843.
85 S. Liaquat, S. Farrukh, N. Ahmad, S. S. Karim, E. Pervaiz, A. Sultan and S. Ali, *Environ. Sci. Water Res. Technol.*, 2024, **10**, 1637–1652.
86 O. A. Attallah, M. A. Al-Ghobashy, M. Nebsen and M. Y. Salem, *RSC Adv.*, 2016, **6**, 11461–11480.
87 A. Qureashi, A. H. Pandith, A. Bashir, T. Manzoor, L. A. Malik and F. A. Sheikh, *Surf. Interfaces*, 2021, **23**, 101004.
88 D. Portilla, A. Velázquez-López, R. Escobedo and H. Yee-Madeira, *AIMS Mater. Sci.*, 2024, **11**(4), 991–1012.
89 D. Jiang, Y. Huan, C. Sun, C. Hu, J. Guo, J. Long, M. A. Khan, D. P. Young and Z. Guo, *RSC Adv.*, 2016, **6**, 91584–91593.
90 A. M. Predescu, E. Matei, A. C. Berbecaru, C. Pantilimon, C. Drăgan, R. Vidu, C. Predescu and V. Kuncser, *R. Soc. Open Sci.*, 2018, **5**, 171525.
91 A. Mohamed, R. Atta, A. A. Kotp, F. I. Abo El-Ela, H. Abd El-Raheem, A. Farghali, D. H. M. Alkhalifah, W. N. Hozzein and R. Mahmoud, *Sci. Rep.*, 2023, **13**, 7227.
92 D. Kovář, A. Malá, J. Mlčochová, M. Kalina, Z. Fohlerová, A. Hlaváček, Z. Farka, P. Skládal, Z. Starčuk and R. Jiřík, *J. Nanomater.*, 2017, **2017**(1), 7859289.
93 Y. Sehlleier, S. Hardt, C. Schulz and H. Wiggers, *J. Environ. Chem. Eng.*, 2016, **4**, 3779–3787.
94 R. K. Wardani, K. Dahlan, S. T. Wahyudi and S. G. Sukaryo, *AIP Conf. Proc.*, 2019, **2194**(1), 020137.
95 N. Mufti, D. Sari, A. Muyasaroh and A. Taufiq, *J. Phys.:Conf. Ser.*, 2020, **1595**(1), 012004.
96 K. Y. Kumar, H. Muralidhara, Y. A. Nayaka, J. Balasubramanyam and H. Hanumanthappa, *Powder Technol.*, 2013, **246**, 125–136.
97 A. K. Badawi, M. Abd Elkodous and G. A. Ali, *RSC Adv.*, 2021, **11**, 36528–36553.
98 R. Jayalakshmi, J. Jeyanthi and K. A. Sidhaarth, *Environ. Nanotechnol. Monit. Manag.*, 2022, **17**, 100659.
99 V. Chavan, V. Kothavale, S. Sahoo, P. Kollu, T. Dongale, P. Patil and P. Patil, *Phys. B*, 2019, **571**, 273–279.
100 P. B. Patil and V. P. Kothavale, *Advances in Metal Oxides and Their Composites for Emerging Applications*, Elsevier, 2022, pp. 401–424.
101 A. M. Azzam, S. T. El-Wakeel, B. B. Mostafa and M. El-Shahat, *J. Environ. Chem. Eng.*, 2016, **4**, 2196–2206.
102 G. Mohamed, N. Hassan, A. Shahat, A. El-Didamony and A. Ashraf, *Biointerface Res. Appl. Chem.*, 2021, **11**, 13377–13401.
103 M. Ghasemi, S. Mashhadi and J. Azimi-Amin, *J. Water Environ. Nanotechnol.*, 2018, **3**, 321–336.
104 R. M. Cornell and U. Schwertmann, *The Iron Oxides: Structure, Properties, Reactions, Occurrences and Uses*, John Wiley & Sons, 2003.
105 L. Lv, M. P. Hor, F. Su and X. Zhao, *J. Colloid Interface Sci.*, 2005, **287**, 178–184.
106 N. N. Nassar, *J. Hazard Mater.*, 2010, **184**, 538–546.
107 Y. Xie, Q. Rong, C. Wen, X. Liu, M. Hao, Z. Chen, H. Yang, G. I. N. Waterhouse, S. Ma and X. Wang, *CCS Chem.*, 2024, **6**, 1908–1919.
108 S. Chen, R. Ding, B. Li, J. Lu and X. Zhang, *Sep. Purif. Technol.*, 2025, **354**, 129451.
109 R. Ding, Y. Zhu, L. Jing, S. Chen, J. Lu and X. Zhang, *Int. J. Biol. Macromol.*, 2024, **282**, 137037.
110 D. C. Kalyani, A. A. Telke, S. P. Govindwar and J. P. Jadhav, *Water Environ. Res.*, 2009, **81**, 298–307.
111 T. Shen, C. Jiang, C. Wang, J. Sun, X. Wang and X. Li, *RSC Adv.*, 2015, **5**, 58704–58712.
112 R. Extremera, I. Pavlovic, M. R. Pérez and C. Barriga, *Chem. Eng. J.*, 2012, **213**, 392–400.
113 K. Imene, B. C. Eddine, B. A. Salah, B. Riadh, A. Gil, B.-A. Imene, G. Messaoued and B. Mokhtar, *Sep. Purif. Technol.*, 2025, **365**, 132656.
114 K. Wang, Z. Song, Z. Xu, Y. Xi, Y. Cui and H. Zhou, *RSC Adv.*, 2025, **15**, 21121–21132.
115 R. Bozbay and N. Orakdogen, *Int. J. Biol. Macromol.*, 2025, **299**, 140034.
116 S. Kamble, S. Agrawal, S. Cherumukkil, V. Sharma, R. V. Jasra and P. Munshi, *ChemistrySelect*, 2022, **7**, e202103084.